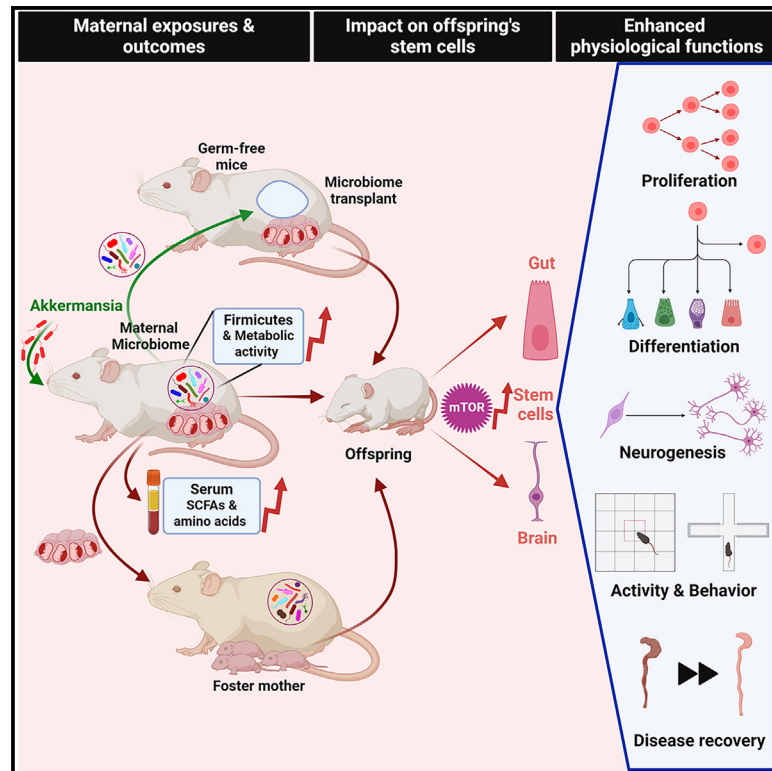


Maternal gut microbiota influence stem cell function in offspring

Graphical abstract



Authors

Haiyue Dang, Panpan Feng, Shuning Zhang, ..., Nick Barker, Philippe Sansonetti, Parag Kundu

Correspondence

parag7777@gmail.com

In brief

Dang et al. demonstrate that maternal gut microbiota during pregnancy program the intestinal and neuronal stem cell characteristics of offspring. This crosstalk between maternal microbiota and fetal stem cells, mediated by circulating metabolites, impacts offspring development, long-term health, behavior, and disease recovery.

Highlights

- Maternal gut microbiota shapes the stem cell characteristics of offspring
- Maternal microbiota during pregnancy have lasting impacts on offspring physiology
- Metabolites from maternal microbiota during pregnancy program offspring stem cells
- The maternal microbiota-stem cell axis in offspring is driven by the mTOR pathway

Article

Maternal gut microbiota influence stem cell function in offspring

Haiyue Dang,^{1,2,3,9} Panpan Feng,^{1,2,3,9} Shuning Zhang,^{1,2,3,9} Lihua Peng,^{1,2} Shuli Xing,^{1,2} Yuchen Li,^{1,2} Xiang Wen,¹ Liqiang Zhou,⁴ Shyamal Goswami,¹ Mingbing Xiao,⁵ Nick Barker,⁶ Philippe Sansonetti,^{7,8} and Parag Kundu^{1,2,3,10,*}

¹Laboratory for Microbiota-Host Interactions, The Center for Microbes, Development and Health, Shanghai Institute of Immunity and Infection, Chinese Academy of Sciences, Shanghai 200031, China

²Institut Pasteur of Shanghai-Chinese Academy of Sciences, Shanghai 200031, China

³University of Chinese Academy of Sciences, Beijing 100039, China

⁴Shanghai Institute of Stem Cell Research and Clinical Translation, Shanghai East Hospital, School of Medicine, Tongji University, Shanghai 200120, China

⁵Department of Gastroenterology, Affiliated Hospital of Nantong University, Nantong 226001, China

⁶Institute of Molecular and Cell Biology, Singapore and Department of Physiology, Yong Loo Lin School of Medicine, National University of Singapore, Singapore

⁷The Center for Microbes, Development and Health, Institut Pasteur of Shanghai-Chinese Academy of Sciences, Shanghai 200031, China

⁸Present address: Institut Pasteur, 75015 Paris, France

⁹These authors contributed equally

¹⁰Lead contact

*Correspondence: parag7777@gmail.com

<https://doi.org/10.1016/j.stem.2024.10.003>

SUMMARY

The maternal microbiome influences child health. However, its impact on a given offspring's stem cells, which regulate development, remains poorly understood. To investigate the role of the maternal microbiome in conditioning the offspring's stem cells, we manipulated maternal microbiota using *Akkermansia muciniphila*. Different maternal microbiomes had distinct effects on proliferation and differentiation of neuronal and intestinal stem cells in the offspring, influencing their developmental trajectory, physiology, and long-term health. Transplantation of altered maternal microbiota into germ-free mice transmitted these stem cell phenotypes to the recipients' offspring. The progeny of germ-free mice selectively colonized with *Akkermansia* did not display these stem cell traits, emphasizing the importance of microbiome diversity. Metabolically more active maternal microbiomes enriched the levels of circulating short-chain fatty acids (SCFAs) and amino acids, leaving distinct transcriptomic imprints on the mTOR pathway of offsprings' stem cells. Blocking mTOR signaling during pregnancy eliminated the maternal-microbiome-mediated effects on stem cells. These results suggest a fundamental role of the maternal microbiome in programming offsprings' stem cells and represent a promising target for interventions.

INTRODUCTION

The gut microbiota, a complex ecosystem of microbial communities residing in the gut, orchestrates an intricate interplay driving host physiology and organ functions.¹ We and others have demonstrated that gut microbiome, the prokaryotic counterpart of “the holobiont,” regulates diverse physiological processes of its eukaryotic host, including organ maturation and function and aging.^{1–4} The gut microbiome displays distinct compositional and functional features depending on host age, health status, and physiological states such as pregnancy. Notably, the maternal gestational gut microbiota features hallmark characteristics essential for proper conditioning of the offspring's health.¹ It is now established that the maternal microbiome can influence multiple developmental aspects of the offspring, such as immune- and neuro-development, and meta-

bolic phenotypes,^{5–9} which likely have long-term health implications. By contrast, disruption in the maternal microbiome severely affects the developmental processes of the offspring, leading to neuro- and intestinal-developmental disorders and inflammation.^{10–12} Together, these findings implicate maternal microbiota as a critical determinant for offspring's development and health as well as its predisposition to develop disease later in life.

Pre- and postnatal development of all complex organisms is essentially governed by processes such as cellular proliferation, growth, and differentiation. Stem cells, which possess enormous self-renewal capacity, typically regulate these key developmental processes.¹³ During postnatal life, different categories of stem cells continue to replenish the cellular requirements for tissue and organ maturation, aiding in the development of a healthy body. Thus, the maternal microbiome and offspring's

stem cells are *bona fide* candidates that seem to play central roles governing early life development, underscoring a possible “microbiome-stem cell axis” regulating development. Although several studies have addressed the role of maternal microbiome on offspring’s immune and metabolic health, its influence on the stem cells and associated developmental processes of the offspring remain obscure.

RESULTS

Early life exposure to *Akkermansia muciniphila* influences neuronal and intestinal stem cells

The capacity to generate new cells—i.e., “proliferation”—and form different types of cells—i.e., “differentiation”—are hallmark characteristics of stem cells that essentially control growth, development, and organ maturation during early life.¹⁴ This prompted us to closely scrutinize how alterations in the microbiome during early life affect these crucial stem cell functions of the offspring. We chose *Akkermansia muciniphila* (Am) for this purpose based on its established capacity to modify the gut microbiota and its potential as a next-generation probiotic.^{15,16} To assess the effects of microbiome on offspring’s stem cells, we exposed mice during the entire pregnancy period and subsequently the newborns to *Akkermansia muciniphila* (Figure S1A). Mice receiving vehicle served as experimental controls. We focused on assessing proliferation and neurogenesis in the offspring’s brain, particularly in the hippocampus, given its critical role in development and its significance as a hotspot for adult neurogenesis. Offspring exposed to Am during early life had more Minichromosome Maintenance Complex Component 2 (MCM2)-positive cells in the dentate gyrus of the hippocampus, indicating increased proliferation in the brain (Figures S1B and S1C). A parallel increase in the number of doublecortin-positive (DCX+) neurons was observed in the dentate gyrus of the hippocampus of Am-exposed mice, suggesting increased neurogenesis (Figures S1D and S1E). Additionally, we detected a higher expression of hippocampal CD133, the marker for cellular stemness in the Am-exposed mice compared with controls (Figure S1F). However, the morphology, number, and soma size of microglia, the key immune cells in the brain, were similar between the two groups (Figures S1G–S1I). While the hippocampal expression of tight junction markers such as claudin 1 and occludin was similar between the groups, we observed a modest increase in zonula occludens (ZO)-1 in the Am-exposed mice (Figures S1J–S1L). This suggests that Am exposure possibly had a subtle influence on the blood-brain barrier, consistent with our previous reports.²

We next questioned if this phenomenon is specific for neuronal stem cells and investigated the effect of Am exposure on intestinal stem cells, which are perpetually regenerative under steady-state conditions in contrast to the neuronal stem cells. We noticed a marked increase in intestinal cellular proliferation, quantified by 5-ethynyl-2'-deoxyuridine (EdU)-marked cells in intestinal Swiss rolls (entire intestine rolled in a spiral configuration allowing unbiased analysis) (Figures S2A and S2B), and growth, characterized by villi lengths, crypt depths, and intestinal lengths in the Am-exposed offspring compared with controls (Figures S2C–S2G). However, the extent of apoptosis in the intestinal milieu was minimal and comparable between the two groups as determined by the terminal deoxynucleotidyl transferase-mediated nick end labeling (TUNEL) assay (Figures S2H

and S2I). Evaluating the differentiation of intestinal cells was a major challenge, given the diverse cell types involved and variations in spatial distribution of specific cellular populations along the length of the intestine. For unbiased assessment, we did multiplex-immunohistochemistry (IHC) of the entire intestinal Swiss rolls from the two groups of offspring, which allows simultaneous staining of multiple biomarkers within a single tissue section. Exhaustive multiplexed-imaging analysis revealed an increase in the intestinal stem cell pool along with an expansion of secretory lineages including goblet, Paneth, and enteroendocrine cells in the Am-exposed offspring compared with controls (Figures S2J–S2N). Quantification of Lgr5 expression in purified crypts further indicated an increase in stem cells in the Am-exposed mice (Figure S3A), while the expression of epithelial markers such as cytokeratin-8 and cytokeratin-20 were similar between the two groups (Figures S3B and S3C). The basal levels of inflammatory markers and junctional proteins, such as interleukin (IL)-17, tumor necrosis factor alpha (TNF- α), occludin, claudin-1, and ZO-1, were comparable between the groups (Figures S3D–S3H), suggesting no obvious difference in intestinal inflammation or barrier integrity.

To further assess the effect of early life Am exposure on stem cells, we isolated small intestinal crypts from the offspring of both groups and assessed their organoids forming capacity. Crypts derived from offspring exposed to Am showed enhanced ability to form organoids (Figures S3I and S3J). Moreover, the size of the organoids generated from offspring exposed to Am was larger along with enhanced budding and proliferation (Figures S3K–S3N).

To validate the specificity of Am in altering these stem cell functions, we exposed a group of mice to another anaerobic commensal, *Bacteroidetes thetaiotaomicron* (Bt) in an identical manner (Figure S4A). Offspring exposed to Bt showed no difference in hippocampal neurogenesis, intestinal proliferation, or cellular populations compared with controls (Figures S4C–S4L), suggesting the phenomenon was Am specific. Of note, offspring exposed to Am showed higher body weight compared with controls (Figure S3O), which was not observed in the Bt-exposed offspring (Figure S4B). Collectively, these alterations in neurogenesis, proliferation, and cellular populations in the gut and brain of offspring exposed to Am indicate a distinct influence of early life gut microbiota shifts on the offspring’s stem cells. Nevertheless, these findings raised one key question: whether these alterations in the offspring’s stem cell functions were due to alterations in the maternal microbiome induced by Am or postnatal exposure to Am or a combination of both.

Alteration in gut microbiota during pregnancy is critical for influencing the offspring’s neuronal and intestinal stem cells

To determine the precise cause of these changes in the offspring’s stem cell functions, we exposed mice to Am or PBS during the entire period of pregnancy. Subsequently, the newborn pups from each group were exposed to either PBS or Am from postnatal day 5 and meticulously monitored for their stem cell functions during the initial development phases (Figure 1A). A significant rise in hippocampal neurogenesis, coupled with increased populations of stem cells, goblet cells, and enteroendocrine cells, and heightened intestinal proliferation was

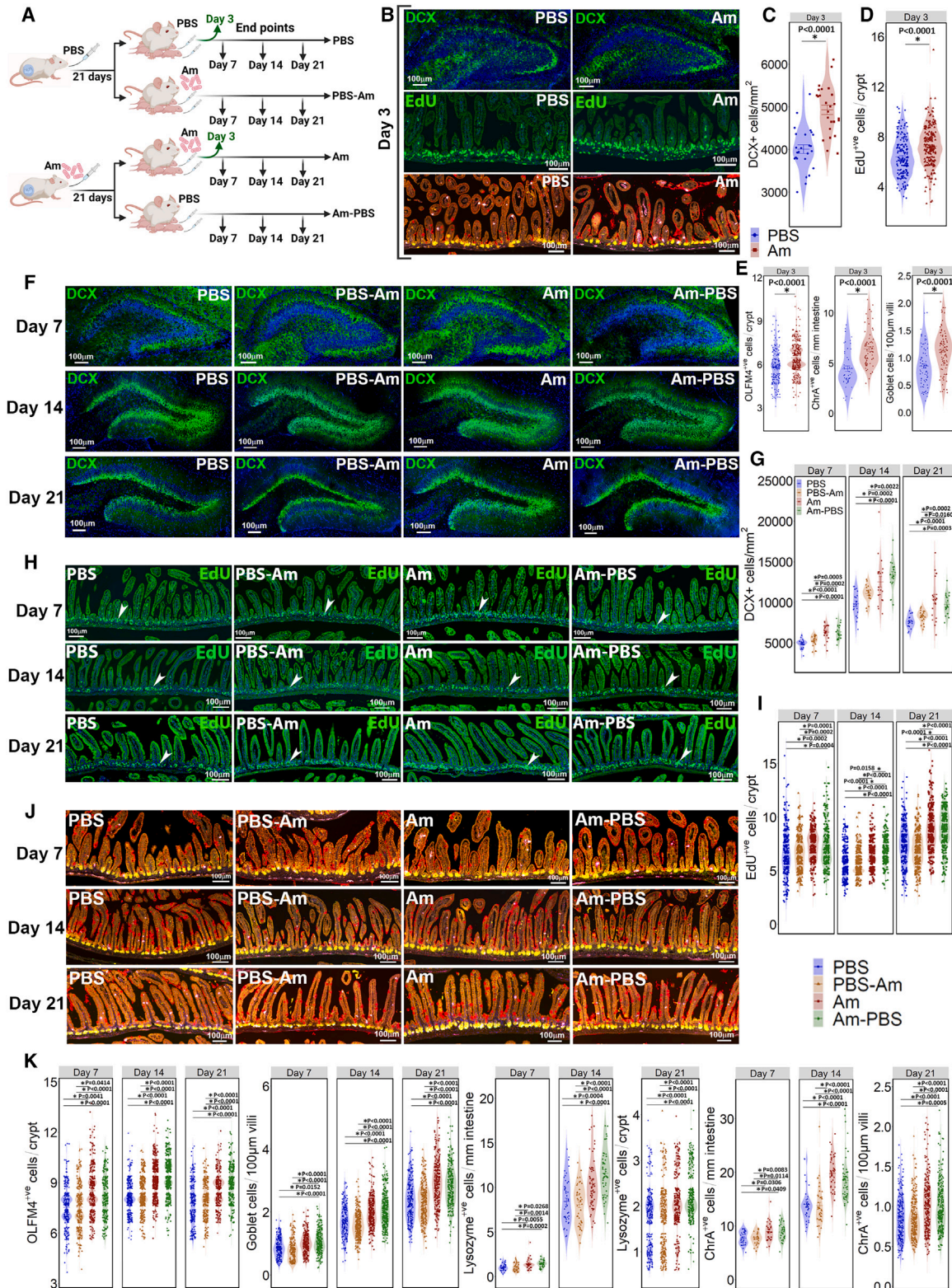


Figure 1. Maternal microbiome dictates the characteristics of neuronal and intestinal stem cells in the offspring during early development (A) Mice were gavaged every alternate day with PBS or Am during the entire period of pregnancy, and the newborn pups from each group were further exposed to either PBS or Am every alternate day from postnatal day 5 till weaning (21 days). The offspring were harvested at postnatal days 3, 7, 14, and 21, respectively.

(legend continued on next page)

evident in the progeny of mothers exposed to Am as early as postnatal day 3 when compared with controls (Figures 1B–1E, S5A, and S5B). Furthermore, the extent of hippocampal neurogenesis during postnatal days 7, 14, and 21 in the offspring from mothers exposed to Am was significantly greater than that observed in the offspring born to PBS-treated mothers, regardless of their postnatal interventions (Figures 1F and 1G). The progeny of Am-exposed mothers also showed a consistent increase in neuronal and intestinal proliferation during early postnatal developmental days compared with those born to vehicle-treated mothers, irrespective of their postnatal exposures (Figures 1H, 1I, S6C, and S6D). We noticed a simultaneous expansion in the populations of stem cells, Paneth cells, goblet cells, and enteroendocrine cells in the intestines of offspring born to Am-exposed mothers compared with the progeny from vehicle-treated mothers, independent of postnatal treatments (Figures 1J, 1K, S5C, S6A, S6B, and S6E). Taken together, these exhaustive comparisons between offspring that were distinctly exposed both prenatally and postnatally revealed a characteristic developmental trajectory for progeny of mothers exposed to Am during pregnancy, clearly differentiating them from those born to vehicle-treated mothers, irrespective of postnatal treatments (Figures 1, S5, and S6). These differences in the developmental trajectory uniquely illustrate the crucial role of the maternal microbiome in programming the offspring's stem cells.

Offspring of mothers with altered microbiota maintained their unique stem cell characteristics even when raised by foster mothers

To affirm that the changes in stem cell characteristics in the offspring of Am mothers were largely due to differences in the microbiota during pregnancy, we isolated 19-day-old embryos from PBS- or Am-exposed pregnant mothers via C-section, revived them, and fostered them with Institute for Cancer Research (ICR) mice housed under similar environmental conditions (Figure 2A). Interestingly, even when fostered, the offspring of Am-exposed mothers (Am-Fs) still displayed elevated numbers of MCM2+ and DCX+ cells in the dentate gyrus of the hippocampus compared with those born to PBS-exposed mothers (PBS-Fs) (Figures 2B–2E). In line, we observed increased intestinal lengths, proliferation, and elevated populations of stem cells, differentiated goblet cells, Paneth cells, and enteroendocrine cells in the Am-Fs compared with PBS-Fs (Figures 2F–2M). Additionally, intestinal organoids derived from purified crypts ex-

hibited higher proliferation rates in Am-Fs compared with PBS-Fs (Figures 2N and 2O). These findings suggest that the stem cell characteristics of offspring are primarily shaped by the maternal microbiome during pregnancy, while changes in breastmilk composition resulting from alterations in the maternal microbiome have minimal influence on this process.

The maternal microbiome has a long-term impact on the offspring's stem cell functions and physiology

We next sought to validate whether alterations in the maternal microbiome had a sustained impact on the stem cells of the offspring, considering that stem cells are inherently long lived and their functions are influenced by previous experiences.^{17–19} We first confirmed the direct impact of maternal microbiome on offspring's stem cells using a non-variegated reporter-based *in vivo* lineage-tracing mouse line, *Lgr5-2A-CreERT2-R26-tdTomato*.²⁰ *Lgr5-2A-CreERT2-R26-tdTomato* mice were exposed to Am or PBS, and we traced the cellular lineage of the gut of their progeny during postnatal development (Figure S7A). Offspring of mothers exposed to Am consistently displayed greater number of Tomato-expressing cells in their intestines, both at 48 and 72 h post tamoxifen treatments compared with control mothers (Figures 3A, 3B, and S7B). In parallel, 6-day-old, matured intestinal organoids from the offspring of each group were exposed to 4-hydroxytamoxifen for 10 h to assess the regenerative capacity of the stem cells. The percentage of Tomato-expressing cells was much higher in the intestinal organoids of offspring born to Am-exposed mothers than those from control mothers (Figures 3C and 3D).

Having confirmed the connection between the maternal microbiome and the offspring's stem cells, we carried out longitudinal studies spanning up to 10 months to assess the long-term impact of the maternal microbiome on the offspring (Figure 3E). Of note, the offspring from each group gained weight during the course of experiment; however, those born to Am-exposed mothers gained less weight than the controls, specifically from about 30 weeks of age (Figure S7C). Surprisingly, the number of DCX+ neurons was greater in the dentate gyri of the offspring born to Am-exposed mothers at 2 months age, and this remained consistent at 5 months and even at 10 months of age, when overall neurogenesis reached its bare minimum, compared with offspring from PBS-treated mothers (Figures 3F and 3G). Likewise, the level of hippocampal proliferation was higher in the offspring of Am-exposed mothers at 2 months of age compared with the control group (Figures S7D and S7E). This

(B) Representative images of hippocampal neurogenesis (upped), intestinal proliferation (middle), and multiplex imaging of intestinal Swiss rolls (lower) from offspring born to PBS- or Am-exposed mothers at postnatal day 3 ($n = 5$ per group). Scale bar, 100 μm .

(C–E) Quantification of hippocampal neurogenesis (C), intestinal proliferation (D), and cellular populations in the intestines (E) of the offspring at postnatal day 3 ($n = 5$ per group).

(F) Representative images of DCX-stained cells in the dentate gyri of offspring from the different groups of mice at postnatal days 7, 14, and 21 (blue, DAPI staining; green, DCX staining). Scale bar, 100 μm .

(G) Quantification of DCX-positive cells in the dentate gyri of the different groups of mice ($n = 5$ per group).

(H) Representative images of EdU staining (DAPI staining, blue; EdU staining, green) of intestinal rolls from the different groups of mice at postnatal days 7, 14, and 21. Scale bar, 100 μm . White arrows indicate EdU-positive cells.

(I) Quantification of EdU-incorporating cells in the small intestinal crypts of the different groups of mice ($n = 5$ per group).

(J) Representative images of multispectral imaging of intestinal rolls from the different groups of mice at postnatal days 7, 14, and 21. (Yellow: Olfactomedin 4 [OLFM4]; green: lysozyme; red: muc2; purple: chromogranin A; orange: E-cadherin; and blue: DAPI.) Scale bar, 100 μm ($n = 5$ per group).

(K) Quantification of OLFM4+ve stem cells, goblet cells, Paneth cells, and enteroendocrine cells in the small intestines of the different groups of mice ($n = 5$ per group). Data are reported as means \pm SEMs. * p calculated using the ANOVA with Tukey's multiple comparisons test and mentioned wherever it is <0.05 .

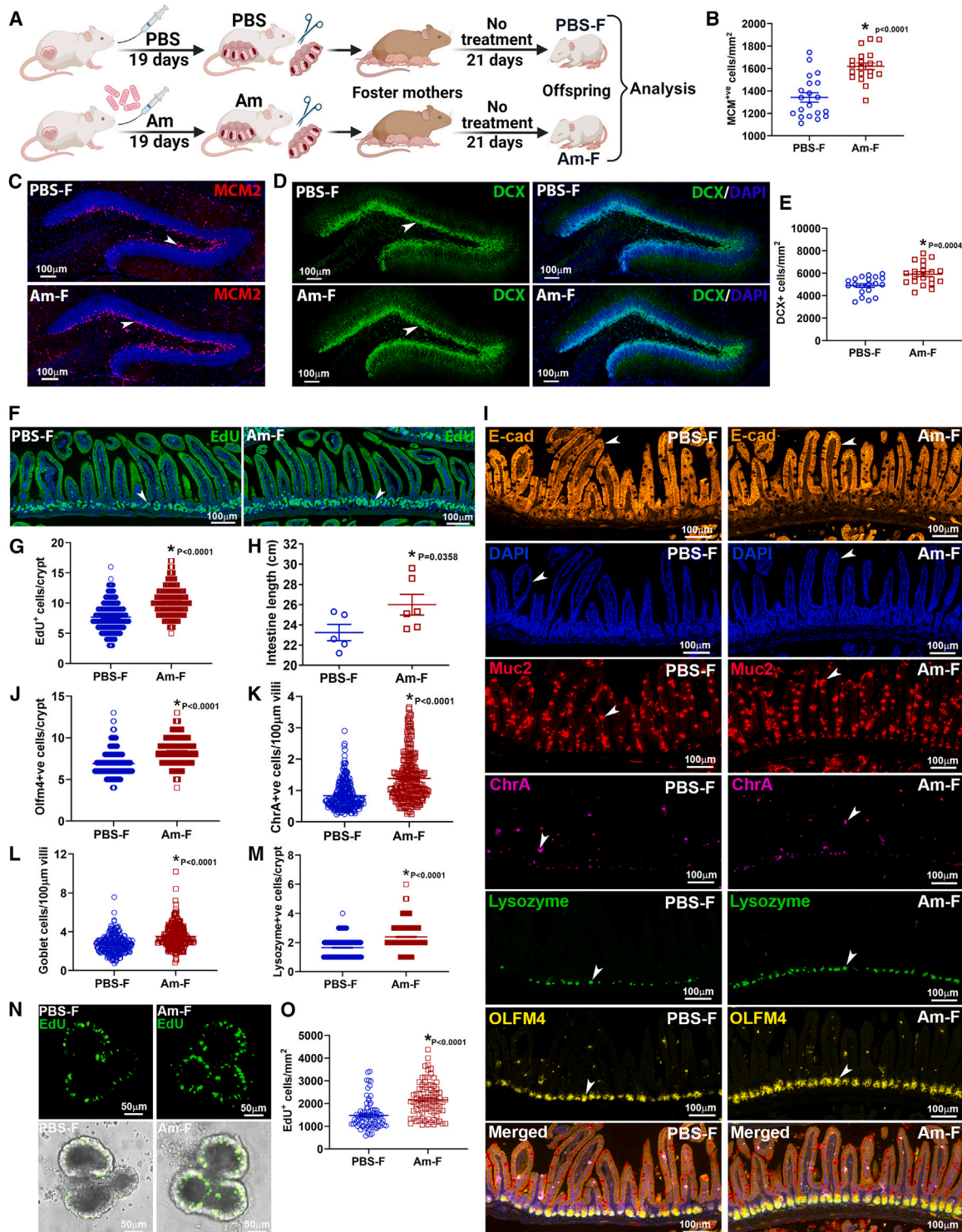


Figure 2. Offspring born to PBS- or Am-exposed mothers retained their distinct stem cell characteristics when raised by foster mothers
(A) Embryos (19-day-old) from pregnant C57BL/6 mice, treated with either PBS or Am, were isolated by C-section, revived, and transferred to foster mothers (ICR mice). The pups from each group were then raised by the foster mothers (referred to as PBS-F and Am-F) until they reached 3 weeks of age.
(B) Quantification of MCM2-positive cells in the dentate gyri of PBS-Fs and Am-Fs ($n = 5$ per group).
(C) Representative images of MCM2-stained cells in the dentate gyri of the two groups of mice (blue, DAPI staining; red, MCM2 staining). Scale bar, 100 μm . White arrows indicate MCM2-positive cells.

increase in hippocampal proliferation was sustained even at 10 months of age (Figures S7D and S7E). We questioned the physiological relevance of these changes in the brain and subjected these mice to a battery of behavioral tests. Remarkably, the progeny of mothers exposed to Am exhibited lower anxiety levels, as they made more entries and spent longer durations in the open arms of the elevated plus maze, compared with the controls (Figures 3H and 3I). Moreover, the progeny of Am-exposed mothers displayed increased locomotory and exploratory behavior by spending longer time in the center of the open field as detected by their movement tracks (Figures 3J and 3K). However, no notable differences in behavioral phenotypes were observed in the light/dark box and Y-maze tests between the two groups (Figures S8A–S8D).

Our prospective studies further revealed a significant surge in intestinal proliferation and an expansion in the populations of stem cells, Paneth cells, goblet cells, and enteroendocrine cells in the offspring born to Am-exposed mothers at 2 months age, which remained consistent later in life (Figures 4A–4G and S9). In addition, we examined the intestinal permeability, a critical physiological parameter, which depends on cellular regeneration and determines overall health, in these mice. Under our experimental setting, we observed a noticeable reduction in intestinal permeability in the progeny of Am-exposed mothers, as indicated by lower serum concentrations of fluorescein isothiocyanate (FITC) dextran compared with controls (Figure 4H). To further assess the regenerative and reparative capacity of stem cells in the offspring, we challenged 2-month-old male offspring of PBS- or Am-exposed mothers with 2.5% dextran sodium sulfate (DSS) for 7 days, which typically induces colitis, and then allowed them to recover for a week (Figure 4I). Shortening and thickening of the colon are typical characteristics of colitis severity. Unexpectedly, we observed that the colons of offspring born to Am-exposed mothers were longer than offspring of PBS-exposed mothers after 7 days of DSS exposure (Figures S8E and S8F), suggesting that changes in maternal microbiomes during pregnancy may influence offspring's disease susceptibility. We next examined crypt morphology of these mice during the recovery phase. Previous studies indicate the presence of hypertrophic crypts, hallmarked by an elevated number of proliferative cells that facilitate crypt regeneration, during recovery in the distal colon.^{21,22} After a 7-day recovery from DSS injury, we noticed a significant increase in colonic length as well as a higher percentage of hypertrophic crypts in the distal colon of offspring born to Am-exposed mothers compared with those

of PBS-exposed mothers (Figures 4J–4M). This was accompanied by a marked increase in proliferating cells within the colonic crypts in areas undergoing recovery (Figures 4N and 4O), indicating enhanced crypt regeneration in offspring of Am-exposed mothers than those born to PBS mothers. However, body weight gain during DSS recovery was comparable between the two groups (Figure S8G). These results collectively indicate that alterations in the maternal microbiome during pregnancy have a long-term impact on the offspring's stem cells, overall physiology, and disease recovery.

Mice exposed to *Akkermansia muciniphila* display distinct microbiomes and metabolic signatures during pregnancy

In an attempt to understand the mechanisms underlying the differences between the progeny of Am or PBS exposed mothers, we compared the maternal microbiomes. Metagenomic analysis of stool samples collected from PBS- or Am-exposed mothers during late gestation revealed distinct clustering of gut microbiota at the genus level between the groups, as evidenced in the principal coordinate analysis (PCoA) (Figure 5A). A Circos plot emphasized a distinct overrepresentation of Firmicutes, particularly in mothers exposed to Am, when compared with those treated with PBS (Figure 5B). This was further confirmed by an enrichment in bacteria belonging to the Lactobacillaceae and Lachnospiraceae families in the Am-exposed mothers compared with controls (Figures 5C, S10A, and S10B). By contrast, the microbiomes of 3-week-old offspring did not show major differences in taxonomy, except that the offspring born to Am-exposed mothers displayed an overrepresentation of *Akkermansia muciniphila* in their metagenome compared with controls (Figures S10C–S10F).

Unbiased functional analysis of the entire cohort of up- and downregulated genes in the maternal microbiomes revealed a distinct enrichment of genes involved in metabolism, including DNA, RNA, and protein metabolism, amino acids and derivatives, carbohydrates, and fatty acids and lipids in mothers exposed to Am, as indicated in the functional network and heatmap (Figures 5D, 5E, and S10G). Furthermore, there was a noticeable enhancement in the butyrate pathway (Figure S10H). We speculated that alterations in the functional profile of the maternal microbiome could influence the composition of metabolites circulating in the mothers, considering the substantial contribution of microbial metabolism to the host's metabolite profile. As expected, targeted metabolomics revealed distinct

(D) Representative images of DCX-stained cells in the dentate gyri of PBS-Fs and Am-Fs (blue, DAPI staining; green, DCX staining). Scale bar, 100 μ m. White arrows indicate DCX-positive cells.

(E) Quantification of DCX-positive cells in the dentate gyri of the two groups of mice ($n \geq 5$ per group).

(F) Representative images of EdU staining (DAPI staining, blue; EdU staining, green) of intestinal rolls of PBS-Fs and Am-Fs. Scale bar, 100 μ m. White arrows indicate EdU-positive cells.

(G) Quantification of EdU-incorporating cells in the small intestinal crypts ($n = 5$ per group).

(H) Intestinal lengths of PBS-Fs and Am-Fs ($n \geq 5$ per group).

(I) Representative images of multispectral imaging of intestinal rolls from PBS-Fs and Am-Fs (yellow: OLFM4; green: lysozyme; red: muc2; purple: chromogranin A; orange: E-cadherin; and blue: DAPI). Scale bar, 100 μ m. White arrows indicate cells stained for respective markers.

(J–M) Quantification of OLFM4+ve stem cells (J), enteroendocrine cells (K), goblet cells (L), and Paneth cells (M) in the small intestines of the two groups of mice ($n = 5$ per group).

(N) Representative images of EdU staining (DAPI staining, blue; EdU staining, green) of organoids from PBS-Fs and Am-Fs. Scale bar, 50 μ m.

(O) Quantification of EdU-incorporating cells in the organoids from the two groups. Data are reported as means \pm SEMs. * p calculated using the Student's t test and mentioned wherever it is <0.05 .

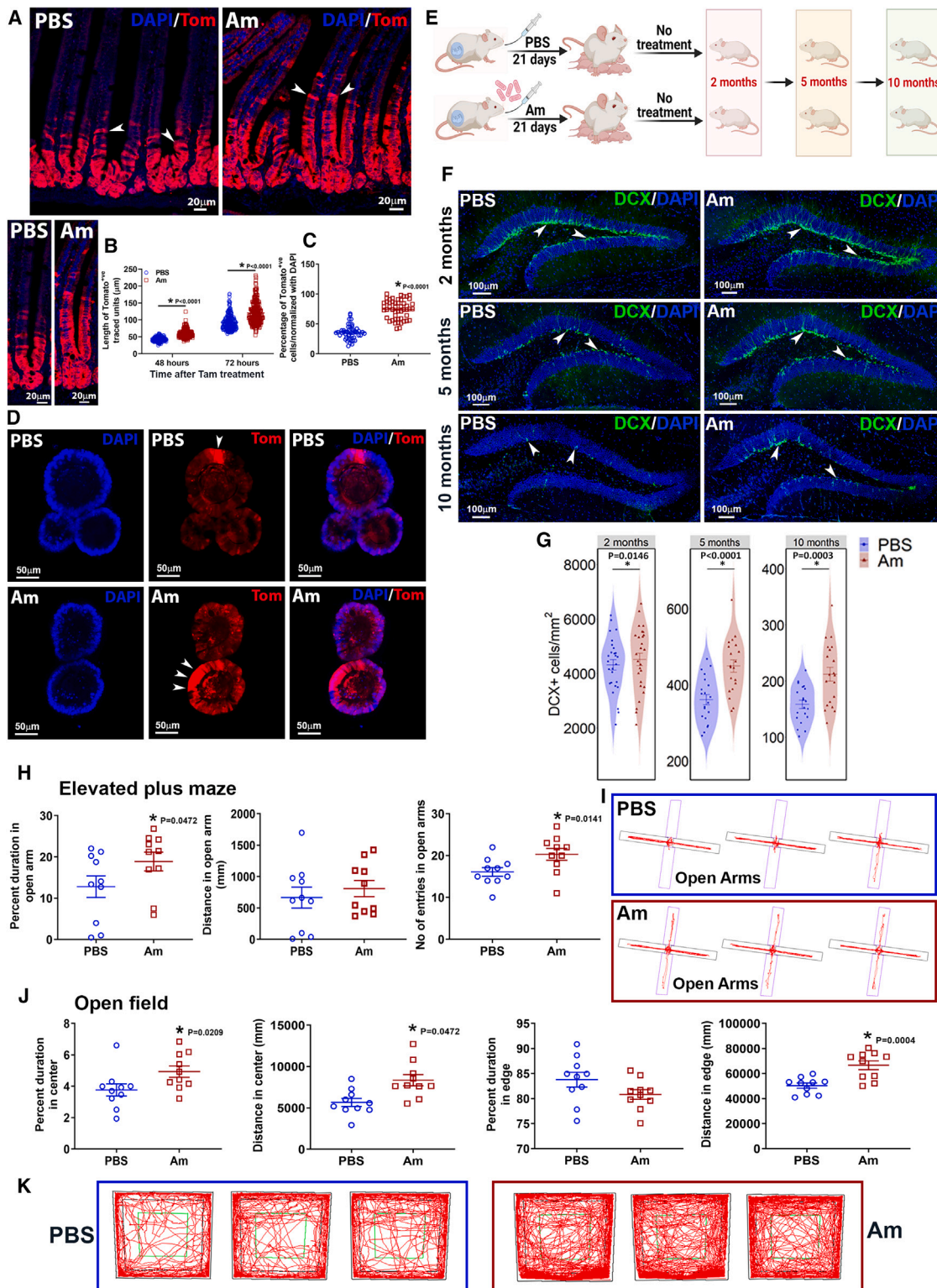


Figure 3. Maternal microbiome has a long-term impact on the offspring's neuronal stem cells and behavior

(A) Representative images showing expression of Tomato in the intestines of 21-day-old offspring groups, 3 days post tamoxifen administration (blue, DAPI staining; red, Red Fluorescent Protein [RFP] staining) ($n = 5$ per group). White arrows indicate Tomato-positive cells. Scale bar, 20 μm .
 (B) The distance of traced Tomato-positive cells was scored along the crypt-villi axis in the two groups at 48 or 72 h post tamoxifen treatment ($n = 5$ per group).
 (C) The percentage of Tomato-positive cells in organoids cultured from the small intestines of the two groups of mice.

differences in the metabolic signatures between mothers exposed to Am versus those treated with the vehicle (Figures 5F and 5G). Mothers exposed to Am appeared to be metabolically more active, exhibiting higher levels of short-chain fatty acids (SCFAs), such as propionic acid, acetic acid, and butyric acid derivatives, in their serum (Figure 5G). Additionally, elevated levels of amino acids, such as glycine, glutamine, and arginine, and amino acid precursors, like citrulline and oxaloacetic acid, were detected in their serum compared with controls (Figure 5G). Interestingly, we also noticed diminished levels of adenosine monophosphate in their serum, indicating a higher energy status than the controls (Figure 5G). The distinct metabolomic signatures in the serum of the Am and PBS-exposed mothers prompted us to test their biological activity. We exposed the 6-day-old culture of human organoids to serum from either Am- or PBS-treated mothers. Surprisingly, human organoids treated with serum from Am-exposed mothers exhibited increased cellular proliferation in contrast to PBS controls (Figures 5H and 5I). To further confirm whether the stem cells were affected by this metabolite enrichment, we exposed mature organoids from *Lgr5-2A-CreERT2-R26-tdTomato* mice to serum from the two groups of mothers. A 10-h exposure markedly increased the percentage of Tomato-expressing cells in the intestinal organoids exposed to serum from Am-exposed mothers than those from control mothers (Figures 5J and 5K).

Considering the specific enrichment of SCFAs and amino acids in the serum of Am-exposed mothers, we next subjected wild-type and *Lgr5-2A-CreERT2-R26-tdTomato* mice to a high-fiber, high-protein (HFHP) diet (Table S1), during the entire period of pregnancy. Interestingly, serum from wild-type pregnant mothers fed with HFHP diet increased the percentage of Tomato-expressing cells in the *Lgr5-2A-CreERT2-R26-tdTomato* mouse organoids to a similar extent to those exposed to serum from Am-exposed mothers (Figures S11A and S11B). Additionally, the offspring of HFHP diet-fed *Lgr5-2A-CreERT2-R26-tdTomato* mice displayed increased lengths of Tomato-traced units in their intestines compared with the offspring of PBS-exposed mothers; however, this increase was less pronounced than in those born to Am-exposed mothers at 72 h post-tamoxifen treatment (Figures S11C and S11D). These findings not only suggest a potential communication between the gut microbiota and stem cells via circulating metabolites—particularly SCFAs and amino acids—but also underscore the possible role of circulating metabolites in Am-exposed mothers in enhancing their offspring's stem cell functions.

The offspring of GF mice transplanted with microbiota from mothers exposed to Am or PBS phenocopy the progeny of respective donors

We hypothesized that the differences in the stem cell characteristics between the offspring from Am or PBS exposed mothers are possibly due to their unique metagenomic signatures. Thus, we transplanted gut microbiota from 16- to 18-day pregnant Am or PBS exposed donors to germ-free (GF) recipient mice and examined the F1 generation offspring (termed-PBS-MTs/Am-MTs) of the recipients at weaning (Figure 6A). Metagenomic analysis revealed distinct clustering of microbiomes of donors and their corresponding recipients for each group, with clear divergence between the two recipient groups (Figure S12A). Thorough comparisons revealed elevated levels of DCX+ and MCM2+ cells in the dentate gyri of the hippocampus of Am-MTs compared with PBS-MTs (Figures 6B–6E). Similarly, we noticed increased intestinal proliferation and lengths, as well as expanded populations of stem cells and differentiated cells of secretory lineage such as goblet cells, Paneth cells, and enteroendocrine cells in the Am-MTs compared with PBS-MTs (Figures 6F–6M). Moreover, organoids grown from intestinal crypts displayed higher proliferation levels in the Am-MTs compared with PBS-MTs (Figures 6N and 6O). Thus, apparently the Am-MTs phenocopied the stem cell characteristics observed in the offspring of mothers exposed to Am, indicating the potential role of maternal microbiota in shaping these stem cell functions.

We next investigated whether these changes in stem cell traits are solely influenced by the overrepresentation of Am or if they result from Am-induced alterations in the composition of the maternal microbiome, particularly the enrichment of Firmicutes. To address this, we created a Firmicutes-deficient intestinal milieu by mono-colonizing GF mice with *Bacteroidetes thetaiotaomicron* (Bt) and exposing these Bt-mono-colonized mice with Am during the entire period of pregnancy (Bt + Am) (Figure S12B). We subsequently compared the offspring of these mice with offspring of PBS-treated GF mothers and ex-GF mothers transplanted with microbiota from Am-exposed mothers (Am-MTs). Surprisingly, we failed to detect many differences in hippocampal neurogenesis or proliferation between the offspring of GF and Bt + Am mothers (Figures S12C–S12F). Interestingly, the levels of hippocampal neurogenesis and proliferation in the offspring of GF and Bt + Am mothers were considerably less compared with the Am-MTs (Figures S12C–S12F). Similarly, intestinal proliferation and lengths were comparable between the offspring of GF and Bt + Am mothers, but relatively less than the Am-MTs (Figures S12G–S12I). A similar trend was observed for the

(D) Representative images of organoids from *LGR5-2A-creERT2-R26-tdTomato* mice groups, 10 h after 4-hydroxytamoxifen treatment (blue, DAPI staining; red, Tomato). White arrows indicate Tomato-positive cells. Scale bar, 50 μ m.

(E) Mice were gavaged every alternate day with PBS or Am during the entire period of pregnancy, and the offspring were harvested at 2, 5, and 10 months of age, respectively.

(F) Representative images of DCX-stained cells in the dentate gyri of offspring at 2, 5, and 10 months of age (blue, DAPI staining; green, DCX staining). Scale bar, 100 μ m. White arrows indicate DCX-positive cells.

(G) Quantification of DCX-positive cells in the dentate gyri of the different groups of mice ($n = 5$ per group).

(H) Anxiety-like behavior of the offspring at 2 months of age in the elevated plus maze. Plots show the percent time spent in, distance traveled, and the number of entries in the open arms of the elevated plus maze during a 5-min test session ($n = 10$ per group).

(I) Representative tracks showing movement trajectory of mice in the elevated plus maze.

(J) Activity and exploratory behavior in the open field test. Plots show percent duration and distance traveled in the center and percent duration and distance traveled in the edge of the open field during a 20-min test session by the two groups of mice ($n = 10$ per group).

(K) Representative tracks showing movement trajectory of mice in the open field. Data are reported as means \pm SEMs. * p calculated using the Student's t test.

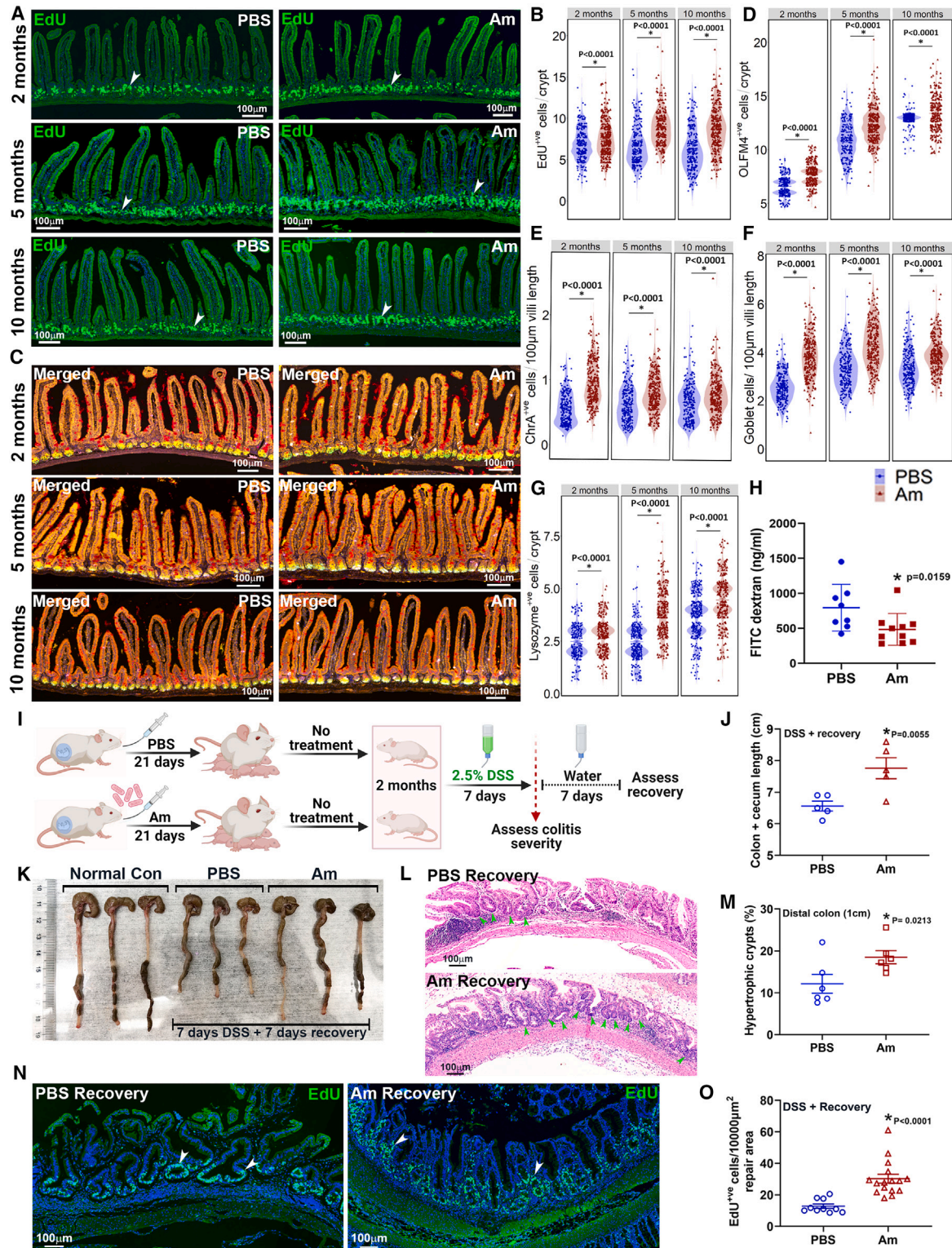


Figure 4. The maternal microbiome has a lasting impact on the intestinal stem cells and physiology of the offspring

(A) Offspring from PBS- or Am-exposed mothers were assessed at 2, 5, and 10 months of age, respectively. Representative images of EdU staining (DAPI staining, blue; EdU staining, green) of intestinal rolls from the different groups of mice. Scale bar, 100 µm. White arrows indicate EdU-positive cells.

(B) Quantification of EdU-incorporating cells in the intestinal crypts of the different groups of mice ($n = 5$ per group).

(C) Representative images of multispectral imaging of intestinal rolls from the different groups of mice. (Yellow: OLFM4; green: lysozyme; red: muc2; purple: chromogranin A; orange: E-cadherin; and blue: DAPI.) Scale bar, 100 µm ($n = 5$ per group).

(legend continued on next page)

population of stem cells and Paneth cells in the offspring of GF and Bt + Am mothers, albeit to a much lesser extent than in Am-MTs (Figures S12J–S12L). Conversely, the population of goblet cells and enteroendocrine cells was higher in the offspring of Bt + Am mothers than the GF offspring, though still lower than in the Am-MTs (Figures S12J, S12M, and S12N). These findings highlight two crucial aspects: firstly, the essential role of the maternal microbiome in shaping the stem cell functions of the offspring, and secondly, the inadequacy of *Akkermansia* in influencing these functions in the absence of a diverse microbiome.

Maternal microbiome influences mTOR signaling in the stem cells of the offspring

The maternal microbiota-driven changes in offspring's stem cells prompted us to further investigate the specific stem cell signaling pathways that are influenced by the microbiome. We isolated intestinal stem cells from 3-week-old Lgr5-EGFP-IRES-creERT2 offspring born to Am or PBS-exposed mothers (Figures 7A and S13A). Of note, the population on Lgr5^{hi} cells was higher in the offspring of Am-exposed mothers compared with those of PBS mothers (Figure S13B). RNA sequencing analysis of Lgr5^{hi} cells revealed distinct transcriptional signatures for signal transduction genes between the two groups of offspring (Figure 7B). Substantial transcriptional variations were observed in molecular pathways related to cellular signaling, proliferation, and growth (Figures 7C and S13C). We specifically noticed an enrichment in genes related to PI3K-Akt-mTOR pathway (Figure 7D), which regulates neurogenesis, cellular growth, and proliferation,^{23–25} in the Lgr5^{hi} cells of offspring born to Am-exposed mothers. The activation levels of mTOR and its downstream target S6 were indeed elevated in the intestinal crypts and hippocampus of 21-day-old offspring born to Am-exposed mothers (Figures 7E–7G and S13D–S13F). Interestingly, increased mTOR activation in the hippocampus and intestines of offspring born to Am-exposed mothers, compared with those of PBS-exposed mothers, was observed as early as postnatal day 3 (Figures S13G–S13I). Multi-color super-resolution imaging further revealed increased co-occurrence of phospho-mTOR specifically in the OLFM4-marked stem cells but not in the neighboring Paneth cells, indicating mTOR activation in the intestinal stem cells of the offspring of Am-exposed mothers (Figures 7H–7J). We observed a similar increase in mTOR activation in the Nestin⁺ neuronal stem/progenitor cells of the progeny of Am-exposed mothers (Figures 7K and 7L).

Inhibition of mTOR signaling during pregnancy abolished the maternal-microbiota-induced stem cell traits

To validate the importance of mTOR pathway in the maternal microbiome driven changes in offspring's stem cell functions, we treated mice with rapamycin, a specific inhibitor of mTOR signaling, in addition to the Am or PBS exposures, throughout the entire pregnancy period (Figure S14A). The body weights of the offspring of the two groups at weaning were similar (Figure S14B). The levels of hippocampal neurogenesis and proliferation were comparable between the two groups of offspring (Figures S14C–S14F). Likewise, intestinal lengths, proliferation, and cellular populations were also comparable between the progeny of the two groups (Figures S14G–S14N). Reasonably, the proliferation levels of intestinal organoids grown from these offspring were also similar (Figures S14O and S14P). Furthermore, rapamycin dose-dependently inhibited the increase in the percentage of Tomato-expressing cells in Lgr5-2A-CreERT2-R26-tdTomato mouse organoids following exposure to serum from Am-exposed mothers (Figures S13J and S13K). Overall, these findings emphasize the crucial role of mTOR signaling in the maternal microbiome-mediated functional changes observed in the offspring's stem cells.

DISCUSSION

Here, we attempted to uncover the functional importance of maternal gut microbiota in regulating the stem cell functions of the offspring by manipulating the maternal microbiome using a health-associated microbe, *Akkermansia muciniphila*. We showed that stem cells in the brain and intestine of the developing offspring responded differently to distinct maternal microbiome signatures. For instance, *Akkermansia*-mediated shifts in maternal microbiota during pregnancy led to changes in stem cell characteristics such as increased hippocampal neurogenesis, neuronal and intestinal proliferation, and altered cellular population dynamics in the intestines of the offspring. These changes in stem cell functions induced by the maternal microbiome resulted in a distinct postnatal developmental trajectory in the progeny. These altered stem cell characteristics were sustained even when the offspring were raised by foster mothers, highlighting the importance of maternal microbiome composition during pregnancy on child health. The changes in these

(D–G) Quantification of OLFM4⁺ stem cells (D), enteroendocrine cells (E), goblet cells (F), and Paneth cells (G) in the small intestines of the different groups of mice ($n = 5$ per group).

(H) Intestinal permeability of the two groups of mice was measured by FITC-dextran translocation to the circulation following oral gavage ($n \geq 8$ per group).

(I) To assess recovery from experimental colitis, 2-month-old male mice born to PBS- or Am-exposed mothers were given 2.5% dextran sodium sulfate (DSS) in their drinking water for 7 consecutive days. After this period, the DSS was replaced with normal drinking water, “washout period,” and the mice were allowed to recover for an additional 7 days.

(J) Quantification of cecum and colon lengths in the two groups of mice ($n = 5$ per group).

(K) Macroscopic images of colons of the two groups of mice after 7 days of recovery. Images of cecums and colons from age- and sex-matched untreated mice serve as controls for reference.

(L) H&E-stained sections of colonic mucosa of offspring born to PBS- or Am-exposed mothers undergoing recovery. Green arrows indicate hypertrophic crypts. Scale bar, 100 μ m.

(M) Percentage of hypertrophic crypts within the distal-most colon (1 cm) of mice from the two groups during recovery.

(N) Representative images of EdU staining (DAPI staining, blue; EdU staining, green) of colonic rolls of offspring undergoing recovery from DSS-induced colitis in different groups. Scale bar, 100 μ m. White arrows indicate EdU-positive cells.

(O) Quantification of EdU-incorporating cells in the recovery areas after washout period ($n = 5$ per group). Data are reported as means \pm SEMs. * p calculated using the Student's t test and mentioned wherever it is <0.05 .

stem cell functions, detected as early as 3 days after birth, were sustained and exerted a significant impact on the offspring's physiology later in life, including behavior, intestinal permeability, and disease recovery. Considering that somatic stem cells are long lived,¹⁸ these findings underscore the possibility of offspring's stem cells to sense maternal microbial cues and reprogram their behavior and functions. Our results align with recent reports indicating dialogs between gut microbiota and neuronal or intestinal stem cells, which fine-tune their long-term functions.^{17,18,26}

We demonstrated that, much like a typical probiotic, *Akkermansia* altered the microbiome landscape during pregnancy, enhancing its metabolic capacity and biological activity. We subsequently established the direct link between maternal microbiota and offspring's stem cells when the progeny of GF mothers, conventionalized with microbiota from mothers exposed to Am or PBS, phenocopied the stem cell traits of those born to their respective donors. Unlike the offspring of GF mothers conventionalized with a complete microbiota from Am-exposed donors, the progeny of Am-exposed, ex-GF mothers with a selective flora did not exhibit drastic changes in stem cell traits. This highlights the critical role of a complex microbiome in influencing stem cell functions. However, *Akkermansia* exposure to mothers with a restricted microbiome elevated the populations of goblet and enteroendocrine cells in the intestines of their offspring, possibly through distinct mechanisms that may not involve a complex microbiome. Recent reports showed similar effects of *Akkermansia* or its components on goblet cell density in adult mice.^{27,28}

The radical shifts in the microbial communities and metabolic signatures in the gut microbiomes of Am-exposed mothers altered the repertoire of their serum metabolites. Enrichment of several metabolites, including SCFAs such as propanoic acid, acetic acid, derivatives of butyric acid, and amino acids like arginine, glycine, and glutamine, was evident in the serum of mothers exposed to Am. Given that gut microbiota significantly contributes to the metabolite pool of its host, the elevated levels of circulating SCFAs in Am-exposed mothers are likely a result of an increased population of SCFA-producing Firmicutes, including Lactobacillaceae and Lachnospiraceae, in their microbiota.^{1,29} These enrichments in the Am-exposed mothers clearly contributed to the biological activity of their serum, as it promoted proliferation in the human

colonic organoids and increased cellular turnover in organoids from lineage-tracing *Lgr5-2A-CreERT2-R26-tdTomato* mice, compared with serum from PBS-treated mothers. The critical role of metabolite enrichment in maternal serum, particularly SCFAs and amino acids, on offspring's stem cell functions was established when serum from mothers fed with an HFHP diet promoted cellular turnover in *Lgr5-2A-CreERT2-R26-tdTomato* mouse organoids to a similar extent as that of Am-exposed mothers.

Apparently, mTOR pathway, a typical metabolic sensor and potential regulator of growth, proliferation, and neurogenesis,^{23–25} in the stem cells of the progeny specifically responded to the altered battery of maternal metabolites. This was established when (1) oral administration of the mTOR-inhibitor rapamycin to Am-exposed mothers abolished the altered stem cell phenotypes in the progeny; and (2) rapamycin blocked the increased cellular turnover induced by Am-exposed mothers' serum in *Lgr5-2A-CreERT2-R26-tdTomato* mouse organoids. The activation of mTOR pathway in the stem cells of the progeny may have been driven by any one or a combination of these possible factors. (1) Elevated levels of maternal SCFAs, including the HDAC inhibitors—acetate, propionate, and butyrate—may have influenced mTOR pathway, as documented previously.^{30,31} (2) Enrichment of amino acids in the serum of Am-exposed mothers, particularly arginine, which is a classical activator of mTOR.²³ (3) Depletion of adenosine monophosphates in the serum of Am-exposed mothers representing higher bioenergetics could repress AMP-activated protein kinase (AMPK), the negative regulator of mTOR pathway.^{3,32} Considering somatic stem cells are long lived, the question of how the changes in mTOR signaling are sustained as imprints in these cells remains a compelling subject for future research.

Overall, our research offers new perspectives on the functional importance of the maternal gut microbiota. We provide evidence on the contribution of the maternal gut microbiome in programming the stem cells of two vital and functionally diverse organs of the offspring, thereby shaping their development and physiology. These findings raise fundamental questions on whether the maternal microbiome affects or imprints other stem cell niches in the offspring such as those in the liver or muscles. Given that several developmental disorders are linked to early pathogen exposure, it is tempting to speculate that dialogs between microbes and stem cells during early life play a crucial

(D) Network analysis based on Sequence Annotation and Exploration Database (SEED)-based functional pathways derived from metagenomic data showing differential abundance of functional genes regulating pathways driving cellular growth and metabolism. The color of nodes represents specific pathways, while the size of nodes is proportional to the normalized (by variance-stabilizing transformation) abundance of genes. The edge width represents the correlation value supporting the connection ($n = 5$ per group).

(E) Heatmap showing the cluster analysis and abundance of sequence reads annotating SEED-based functional pathways that differed significantly between the two groups of pregnant mice, derived from metagenomic data ($n = 5$ per group).

(F) Partial least squares discriminant analysis (PLS-DA) plot showing the clustering of metabolites in the serum of PBS- or Am-exposed pregnant mothers based on targeted metabolomics. Each point represents a sample, and ellipses represent 95% confidence intervals ($n = 5$ per group).

(G) Heatmap showing cluster analysis based on abundance of the differential metabolites in the serum between the two groups of pregnant mice ($n = 5$ per group).

(H) Representative images of EdU staining (green) of human organoids treated with serum from PBS- or Am-exposed mothers. Scale bar, 50 μm .

(I) Quantification of EdU-incorporating cells in human organoids, 24 h after serum exposure.

(J) Representative images of organoids from *LGR5-2A-creERT2-R26-tdTomato* mice after 10 h of exposure to serum from 18-day pregnant mothers exposed to either PBS or Am. The organoids were treated with 4-hydroxytamoxifen immediately before serum exposure (blue, DAPI staining; red, Tomato). White arrows indicate Tomato-positive cells. Scale bar, 50 μm .

(K) The percentage of Tomato-positive cells in the organoids. Data are reported as means \pm SEMs. * p calculated using the Student's t test and mentioned wherever it is <0.05 .

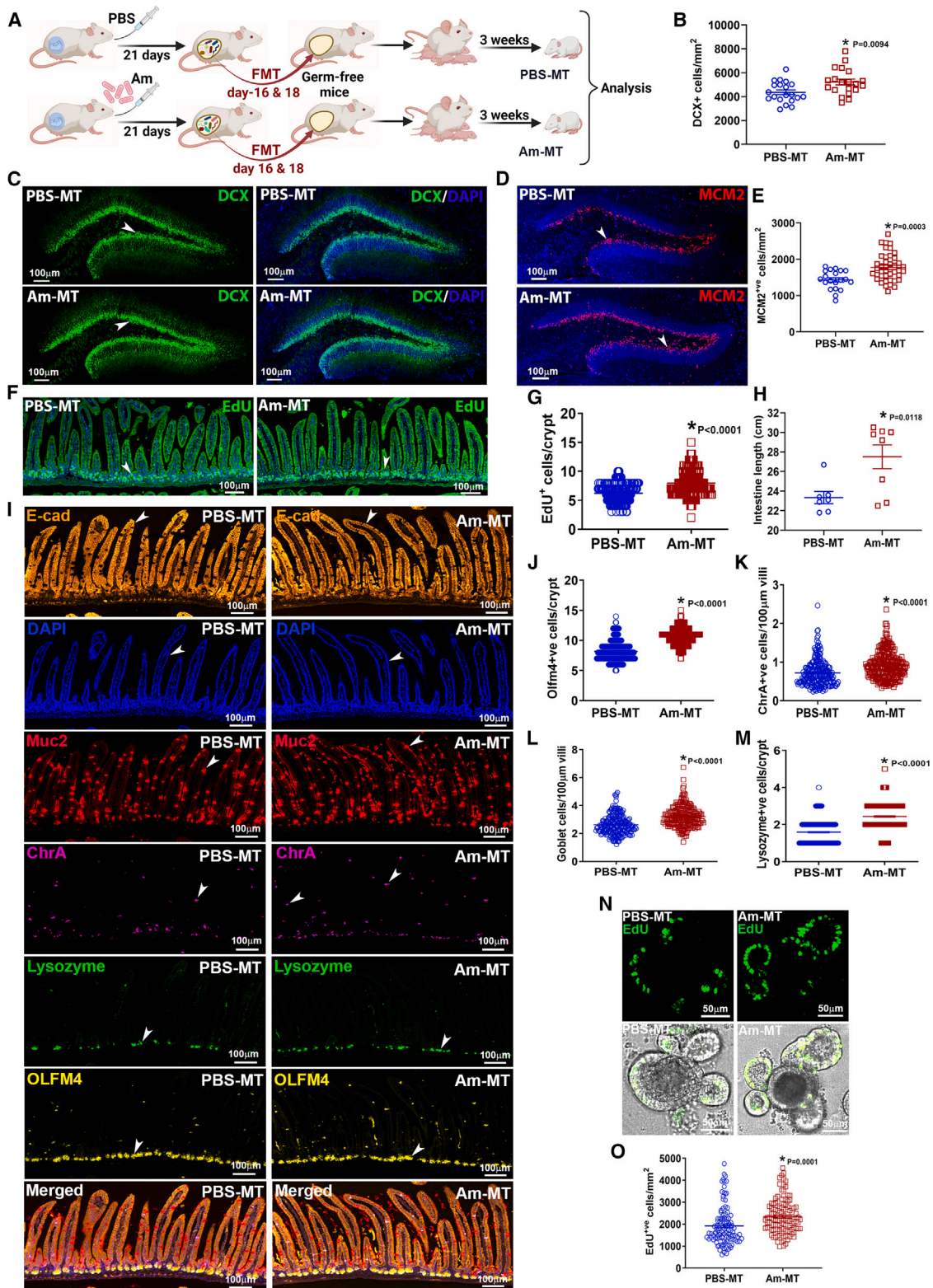


Figure 6. Transplantation of distinct maternal microbiomes into germ-free recipients programs the stem cells of recipients' offspring

(A) Microbiota from PBS- or Am-exposed pregnant (days 16–18) mice were transplanted into ~7-week-old germ-free (GF) recipient mice, which were then housed in a controlled environment till their offsprings reached weaning (21 days). Offsprings from PBS or Am microbiota-transplanted recipient mice are denoted as PBS-MTs or Am-MTs, respectively.

(legend continued on next page)

role in maintaining the delicate balance between health and disease.^{18,33–35} These findings open avenues to support the 21st century medicine in its attempt to develop microbiota-based intervention strategies to promote child health.

Limitations of the study

Our research has limitations owing to its reliance on mouse models, particularly their microbiota composition, as experimental outcomes could be affected by the quality, environment, and hygiene of the facility, which essentially determine the inherent microbiota of the experimental animals it harbors. Considering that stem cells are the cells of origin for several pathological conditions, how maternal microbiome-modulating modalities influence such disease outcomes remains unexplored in this study. Future investigations using genetically engineered mice lacking specific components of stem cells could help pinpoint the interactions between maternal metabolites and nutrient sensors responsible for the observed effects on offspring's stem cells. Finally, extrapolating these findings to humans is crucial and warrants further investigation.

RESOURCE AVAILABILITY

Lead contact

Requests for reagents and resources reported in this article should be directed to and will be fulfilled by Dr. Parag Kundu (parag7777@gmail.com).

Materials availability

The materials, reagents, mouse lines, and original data could also be provided on reasonable request. Some materials would be provided upon completion of Materials Transfer Agreement.

Data and code availability

The raw metagenomic sequencing data for maternal and offspring microbiota have been deposited at NCBI Sequence Read Archive (SRA) database: SRP492208, with accession IDs SRR28131251–SRR28131270. Metagenomics data using fecal samples from PBS/Am mothers are denoted as PBS-M/Am-M, while PBS/Am pups (offspring) are denoted as PBS-P/Am-P, respectively, in the raw files. The raw metagenomic sequencing data for microbiota transplantations from pregnant mothers (donors) to germ-free recipients has been deposited at NCBI SRA database: SRP495394, with accession IDs SRR28352051–SRR28352062. Microbiota donors from each group are denoted as PBS/Am-donor, whereas the recipients are denoted as PBS/Am-recipient, respectively, in the raw files. The raw RNA sequencing

data for purified small intestinal stem cells have been deposited at NCBI SRA database: SRP494239 with accession IDs SRR28277820–SRR28277831. The raw targeted-metabolomics data from maternal serum has been deposited at National Omics Data Encyclopedia (NODE) database, <https://www.biosino.org/node/project/detail/OEP005141>: OEP005141, with accession IDs OER460898–OER460907.

ACKNOWLEDGMENTS

Our studies are supported by the Shanghai Municipal Science and Technology Major Project (project number: 2019SHZDZX02) and the National Natural Science Fund of China (project number: 32150610480). The authors acknowledge Dr. Gediminas Greicius and Pr. Walter Wahli for reviewing the manuscript and critical comments. The authors acknowledge Jinze Li, Chao Shi, and Hong Zou for their help with the animal experimentation.

AUTHOR CONTRIBUTIONS

H.D., P.F., S.Z., L.P., Y.L., X.W., and S.G. performed experiments. H.D. and P.F. analyzed experimental datasets. S.X. and L.Z. analyzed metagenomic datasets. M.X. provided human samples. N.B. provided scientific suggestions and mouse lines and reviewed the manuscript. P.S. provided scientific suggestions and reviewed the manuscript. P.K. conceived and designed the project and wrote the manuscript.

DECLARATION OF INTERESTS

The authors declare no competing interests.

STAR★METHODS

Detailed methods are provided in the online version of this paper and include the following:

- [KEY RESOURCES TABLE](#)
- [EXPERIMENTAL MODEL AND STUDY PARTICIPANT DETAILS](#)
 - Mice
 - Human participant
- [METHOD DETAILS](#)
 - Bacterial culture
 - Isolation of crypts and organoids culture
 - Human organoids and serum exposure
 - Intestinal Permeability Test
 - Behavioral tests
 - Metagenomics
 - Histology
 - In vivo proliferation assay

(B) Quantification of DCX-positive cells in the dentate gyri of PBS-MTs and Am-MTs ($n \geq 5$ per group).

(C) Representative images of DCX-stained cells in the dentate gyri of the two groups of mice (blue, DAPI staining; green, DCX staining). Scale bar, 100 μm . White arrows indicate DCX-positive cells.

(D) Representative images of MCM2-stained cells in the dentate gyri of PBS-MTs or Am-MTs (blue, DAPI staining; red, MCM2 staining). Scale bar, 100 μm . White arrows indicate MCM2-positive cells.

(E) Quantification of MCM2-positive cells in the dentate gyri of the two groups of mice ($n = 5$ per group).

(F) Representative images of EdU staining (DAPI staining, blue; EdU staining, green) of intestinal rolls of PBS-MTs and Am-MTs. Scale bar, 100 μm . White arrows indicate EdU-positive cells.

(G) Quantification of EdU-incorporating cells in the small intestinal crypts ($n = 5$ per group).

(H) Intestinal lengths of PBS-MTs and Am-MTs ($n \geq 7$ per group).

(I) Representative images of multispectral imaging of intestinal rolls from PBS-MTs and Am-MTs (yellow: OLFM4; green: lysozyme; red: muc2; purple: chromogranin A; orange: E-cadherin; and blue: DAPI). Scale bar, 100 μm . White arrows indicate cells stained for respective markers.

(J–M) Quantification of OLFM4+ve stem cells (J), enteroendocrine cells (K), goblet cells (L), and Paneth cells (M) in the small intestines of the two groups of mice ($n = 5$ per group).

(N) Representative images of EdU staining (DAPI staining, blue; EdU staining, green) of organoids from PBS-MTs and Am-MTs. Scale bar, 50 μm .

(O) Quantification of EdU-incorporating cells in the organoids from the two groups. Data are reported as means \pm SEMs. * p calculated using the Student's t test and mentioned wherever it is <0.05 .

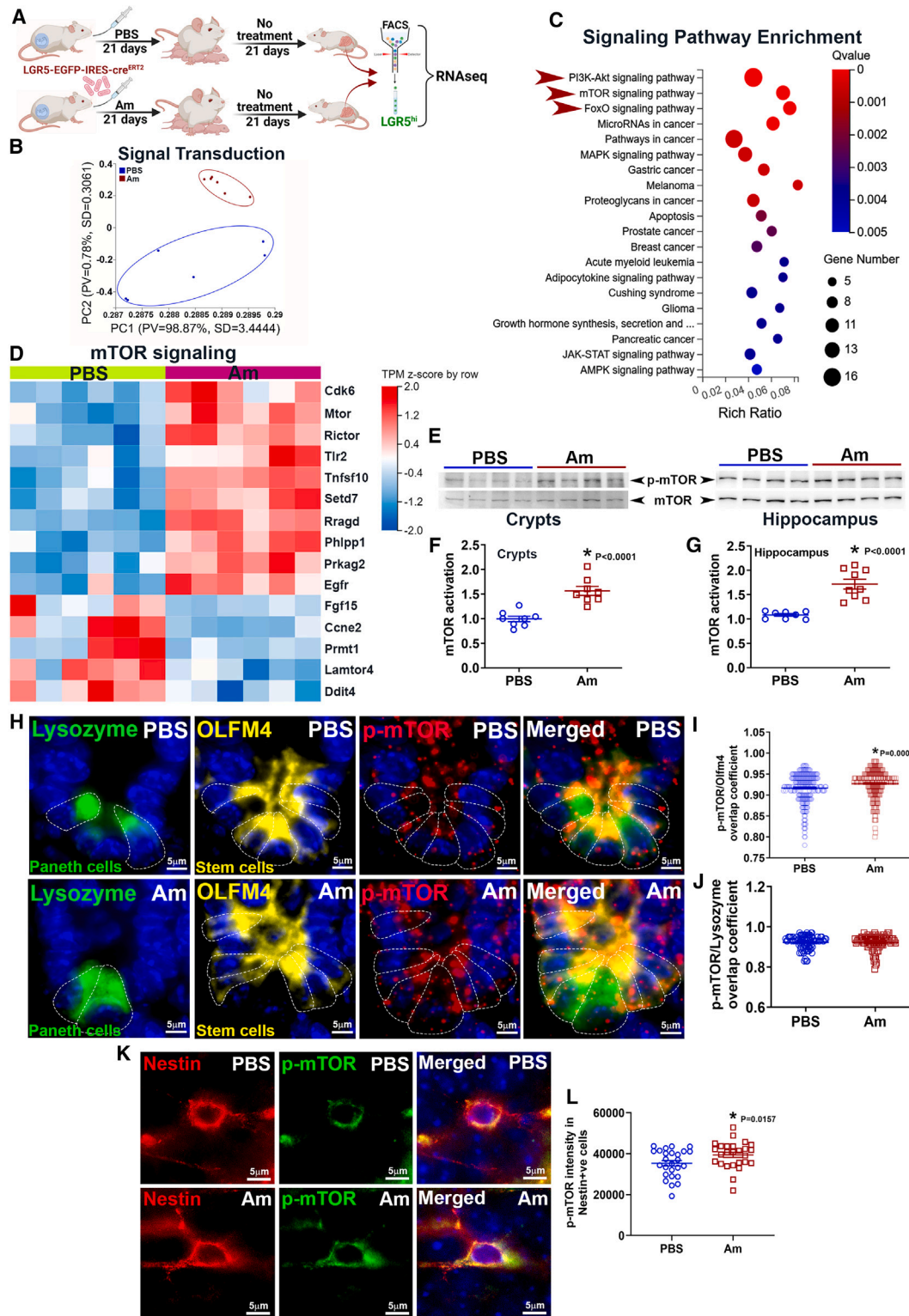


Figure 7. Stem cells from offspring born to mothers with distinct microbiomes exhibit unique characteristics

(A) LGR5-EGFP-IRES-cre^{ERT2} mice were gavaged every alternate day with PBS or Am during the entire period of pregnancy, and the Lgr5⁺ intestinal stem cells from the offspring (day 21) were assessed.

(B) PCA showing distinct clustering of signal transduction genes in the two groups of mice ($n = 6$ per group).

(C) RNA sequencing analysis showing enrichment of signaling pathways in LGR5⁺ intestinal stem cells of the offspring from PBS- or Am-exposed mothers ($n = 6$ per group).

(legend continued on next page)

- Terminal Deoxynucleotidyl Transferase-mediated Nick End Labeling (TUNEL)
- Immunofluorescence staining
- Multiplexed immunohistochemistry staining (mIHC)
- Western blotting
- Real-time PCR
- Targeted Metabolomics
- Sorting of LGR5+ cells and RNA-Seq
- **QUANTIFICATION AND STATISTICAL ANALYSIS**

SUPPLEMENTAL INFORMATION

Supplemental information can be found online at <https://doi.org/10.1016/j.stem.2024.10.003>.

Received: March 19, 2024

Revised: August 29, 2024

Accepted: October 3, 2024

Published: December 11, 2024

REFERENCES

1. Kundu, P., Blacher, E., Elinav, E., and Pettersson, S. (2017). Our gut microbiome: the evolving inner self. *Cell* 171, 1481–1493. <https://doi.org/10.1016/j.cell.2017.11.024>.
2. Braniste, V., Al-Asmakh, M., Kowal, C., Anuar, F., Abbaspour, A., Tóth, M., Korecka, A., Bakocevic, N., Ng, L.G., Kundu, P., et al. (2014). The gut microbiota influences blood-brain barrier permeability in mice. *Sci. Transl. Med.* 6, 263ra158. <https://doi.org/10.1126/scitranslmed.3009759>.
3. Kundu, P., Lee, H.U., Garcia-Perez, I., Tay, E.X.Y., Kim, H., Faylon, L.E., Martin, K.A., Purbojati, R., Drautz-Moses, D.I., Ghosh, S., et al. (2019). Neurogenesis and longevity signaling in young germ-free mice transplanted with the gut microbiota of old mice. *Sci. Transl. Med.* 11, eaau4760. <https://doi.org/10.1126/scitranslmed.aau4760>.
4. Lahiri, S., Kim, H., Garcia-Perez, I., Reza, M.M., Martin, K.A., Kundu, P., Cox, L.M., Selkrig, J., Posma, J.M., Zhang, H., et al. (2019). The gut microbiota influences skeletal muscle mass and function in mice. *Sci. Transl. Med.* 11, eaan5662. <https://doi.org/10.1126/scitranslmed.aan5662>.
5. Gomez de Agüero, M., Ganai-Vonarburg, S.C., Fuhrer, T., Rupp, S., Uchimura, Y., Li, H., Steinert, A., Heikenwalder, M., Hapfelmeier, S., Sauer, U., et al. (2016). The maternal microbiota drives early postnatal innate immune development. *Science* 351, 1296–1302. <https://doi.org/10.1126/science.aad2571>.
6. Kimura, I., Miyamoto, J., Ohue-Kitano, R., Watanabe, K., Yamada, T., Onuki, M., Aoki, R., Isobe, Y., Kashiwara, D., Inoue, D., et al. (2020). Maternal gut microbiota in pregnancy influences offspring metabolic phenotype in mice. *Science* 367, eaaw8429. <https://doi.org/10.1126/science.aaw8429>.
7. Thion, M.S., Low, D., Silvín, A., Chen, J., Grisel, P., Schulte-Schrepping, J., Blecher, R., Ulas, T., Squarzone, P., Hoeffel, G., et al. (2018). Microbiome influences prenatal and adult microglia in a sex-specific manner. *Cell* 172, 500–516.e16. <https://doi.org/10.1016/j.cell.2017.11.042>.
8. Vuong, H.E., Pronovost, G.N., Williams, D.W., Coley, E.J.L., Siegler, E.L., Qiu, A., Kazantsev, M., Wilson, C.J., Rendon, T., and Hsiao, E.Y. (2020). The maternal microbiome modulates fetal neurodevelopment in mice. *Nature* 586, 281–286. <https://doi.org/10.1038/s41586-020-2745-3>.
9. Koren, O., Konnikova, L., Brodin, P., Mysorekar, I.U., and Collado, M.C. (2024). The maternal gut microbiome in pregnancy: implications for the developing immune system. *Nat. Rev. Gastroenterol. Hepatol.* 21, 35–45. <https://doi.org/10.1038/s41575-023-00864-2>.
10. Astbury, S., Song, A., Zhou, M., Nielsen, B., Hoedl, A., Willing, B.P., Symonds, M.E., and Bell, R.C. (2018). High fructose intake during pregnancy in rats influences the maternal microbiome and gut development in the offspring. *Front. Genet.* 9, 203. <https://doi.org/10.3389/fgene.2018.00203>.
11. Kim, E., Paik, D., Ramirez, R.N., Biggs, D.G., Park, Y., Kwon, H.K., Choi, G.B., and Huh, J.R. (2022). Maternal gut bacteria drive intestinal inflammation in offspring with neurodevelopmental disorders by altering the chromatin landscape of CD4(+) T cells. *Immunity* 55, 145–158.e7. <https://doi.org/10.1016/j.immuni.2021.11.005>.
12. Kim, S., Kim, H., Yim, Y.S., Ha, S., Atarashi, K., Tan, T.G., Longman, R.S., Honda, K., Littman, D.R., Choi, G.B., et al. (2017). Maternal gut bacteria promote neurodevelopmental abnormalities in mouse offspring. *Nature* 549, 528–532. <https://doi.org/10.1038/nature23910>.
13. Moore, K.A., and Lemischka, I.R. (2006). Stem cells and their niches. *Science* 311, 1880–1885. <https://doi.org/10.1126/science.1110542>.
14. Sánchez Alvarado, A., and Yamanaka, S. (2014). Rethinking differentiation: stem cells, regeneration, and plasticity. *Cell* 157, 110–119. <https://doi.org/10.1016/j.cell.2014.02.041>.
15. He, X., Bai, Y., Zhou, H., and Wu, K. (2022). Akkermansia muciniphila alters gut microbiota and immune system to improve cardiovascular diseases in murine model. *Front. Microbiol.* 13, 906920. <https://doi.org/10.3389/fmicb.2022.906920>.
16. Cani, P.D., Depommier, C., Derrien, M., Everard, A., and de Vos, W.M. (2022). Akkermansia muciniphila: paradigm for next-generation beneficial microorganisms. *Nat. Rev. Gastroenterol. Hepatol.* 19, 625–637. <https://doi.org/10.1038/s41575-022-00631-9>.
17. Royall, L.N., and Jessberger, S. (2021). How stem cells remember their past. *Curr. Opin. Cell Biol.* 69, 17–22. <https://doi.org/10.1016/j.ceb.2020.12.008>.
18. Naik, S., Larsen, S.B., Cowley, C.J., and Fuchs, E. (2018). Two to tango: dialog between immunity and stem cells in health and disease. *Cell* 175, 908–920. <https://doi.org/10.1016/j.cell.2018.08.071>.
19. Barker, N., van Es, J.H., Kuipers, J., Kujala, P., van den Born, M., Cozijnsen, M., Haegerbarth, A., Korving, J., Begthel, H., Peters, P.J., et al. (2007). Identification of stem cells in small intestine and colon by marker gene Lgr5. *Nature* 449, 1003–1007. <https://doi.org/10.1038/nature06196>.
20. Seishima, R., Leung, C., Yada, S., Murad, K.B.A., Tan, L.T., Hajamohideen, A., Tan, S.H., Itoh, H., Murakami, K., Ishida, Y., et al. (2019). Neonatal Wnt-dependent Lgr5 positive stem cells are essential for uterine gland development. *Nat. Commun.* 10, 5378. <https://doi.org/10.1038/s41467-019-13363-3>.

(D) Heatmap showing enrichment scores for mTOR signaling pathway Kyoto Encyclopedia of Genes and Genomes (KEGG) in the Lgr5+ intestinal stem cells of the two groups of mice. Differential expression analysis was performed using the DESeq2 with false discovery rate (FDR) < 0.001.

(E) Western blot analysis for the activation of mTOR in intestinal crypts and hippocampi of the two groups of offspring (day 21).

(F and G) Quantification of mTOR activation in intestinal crypts (F) and hippocampi (G) of the two groups of offspring ($n \geq 8$ per group).

(H) Representative images of lysozyme, OLFM4, p-mTOR, and DAPI-stained cells in the intestinal crypts from the two groups of mice (yellow: OLFM4; green: lysozyme; red: p-mTOR; and blue: DAPI). Scale bar, 5 μ m.

(I and J) Quantification of mTOR activity in the stem cells (OLFM4+ve) (I) and Paneth cells (lysozyme+ve) (J) of the intestinal crypts in the two groups of mice ($n \geq 5$ per group).

(K) Representative images of Nestin, p-mTOR, and DAPI-stained cells in the hippocampi of the two groups of mice (red: Nestin; green: p-mTOR; and blue: DAPI). Scale bar, 5 μ m.

(L) Quantification of mTOR activity in the neuronal stem cells (Nestin+ve) of hippocampi in the two groups of mice ($n \geq 5$ per group). Data are reported as means \pm SEMs. **p* calculated using the Student's *t* test and mentioned wherever it is < 0.05.

21. Yui, S., Azzolin, L., Maimets, M., Pedersen, M.T., Fordham, R.P., Hansen, S.L., Larsen, H.L., Guiu, J., Alves, M.R.P., Rundsten, C.F., et al. (2018). YAP/TAZ-dependent reprogramming of colonic epithelium links ECM remodeling to tissue regeneration. *Cell Stem Cell* 22, 35–49.e7. <https://doi.org/10.1016/j.stem.2017.11.001>.
22. Wang, Y., Chiang, I.L., Ohara, T.E., Fujii, S., Cheng, J., Muegge, B.D., Ver Heul, A., Han, N.D., Lu, Q., Xiong, S., et al. (2019). Long-term culture captures injury-repair cycles of colonic stem cells. *Cell* 179, 1144–1159.e15. <https://doi.org/10.1016/j.cell.2019.10.015>.
23. Saxton, R.A., and Sabatini, D.M. (2017). *MTOR signaling in growth, metabolism, and disease*. *Cell* 168, 960–976.
24. LiCausi, F., and Hartman, N.W. (2018). Role of mTOR complexes in neurogenesis. *Int. J. Mol. Sci.* 19, 1544. <https://doi.org/10.3390/ijms19051544>.
25. Garza-Lombó, C., and Gonsebatt, M.E. (2016). Mammalian target of rapamycin: its role in early neural development and in adult and aged brain function. *Front. Cell. Neurosci.* 10, 157. <https://doi.org/10.3389/fncel.2016.00157>.
26. Alvarado, A.G., and Lathia, J.D. (2016). Taking a toll on self-renewal: TLR-mediated innate immune signaling in stem cells. *Trends Neurosci.* 39, 463–471. <https://doi.org/10.1016/j.tins.2016.04.005>.
27. Kim, S., Shin, Y.C., Kim, T.Y., Kim, Y., Lee, Y.S., Lee, S.H., Kim, M.N., O, E., Kim, K.S., and Kweon, M.N. (2021). Mucin degrader *Akkermansia muciniphila* accelerates intestinal stem cell-mediated epithelial development. *Gut Microbes* 13, 1–20. <https://doi.org/10.1080/19490976.2021.1892441>.
28. Plovier, H., Everard, A., Druart, C., Depommier, C., Van Hul, M., Geurts, L., Chilloux, J., Ottman, N., Duparc, T., Lichtenstein, L., et al. (2017). A purified membrane protein from *Akkermansia muciniphila* or the pasteurized bacterium improves metabolism in obese and diabetic mice. *Nat. Med.* 23, 107–113. <https://doi.org/10.1038/nm.4236>.
29. Fusco, W., Lorenzo, M.B., Cintoni, M., Porcari, S., Rinninella, E., Kaitsas, F., Lener, E., Mele, M.C., Gasbarrini, A., Collado, M.C., et al. (2023). Short-chain fatty-acid-producing bacteria: key components of the human gut microbiota. *Nutrients* 15, 2211. <https://doi.org/10.3390/nu15092211>.
30. Park, J., Kim, M., Kang, S.G., Jannasch, A.H., Cooper, B., Patterson, J., and Kim, C.H. (2015). Short-chain fatty acids induce both effector and regulatory T cells by suppression of histone deacetylases and regulation of the mTOR-S6K pathway. *Mucosal Immunol.* 8, 80–93. <https://doi.org/10.1038/mi.2014.44>.
31. Zhao, Y., Chen, F., Wu, W., Sun, M., Bilotta, A.J., Yao, S., Xiao, Y., Huang, X., Eaves-Pyles, T.D., Golovko, G., et al. (2018). GPR43 mediates microbiota metabolite SCFA regulation of antimicrobial peptide expression in intestinal epithelial cells via activation of mTOR and STAT3. *Mucosal Immunol.* 11, 752–762. <https://doi.org/10.1038/mi.2017.118>.
32. Noureldein, M.H., and Eid, A.A. (2018). Gut microbiota and mTOR signaling: insight on a new pathophysiological interaction. *Microb. Pathog.* 118, 98–104. <https://doi.org/10.1016/j.micpath.2018.03.021>.
33. Atladóttir, H.O., Thorsen, P., Østergaard, L., Schendel, D.E., Lemcke, S., Abdallah, M., and Parner, E.T. (2010). Maternal infection requiring hospitalization during pregnancy and autism spectrum disorders. *J. Autism Dev. Disord.* 40, 1423–1430. <https://doi.org/10.1007/s10803-010-1006-y>.
34. Jiang, H.Y., Xu, L.L., Shao, L., Xia, R.M., Yu, Z.H., Ling, Z.X., Yang, F., Deng, M., and Ruan, B. (2016). Maternal infection during pregnancy and risk of autism spectrum disorders: A systematic review and meta-analysis. *Brain Behav. Immun.* 58, 165–172. <https://doi.org/10.1016/j.bbi.2016.06.005>.
35. Patterson, P.H. (2009). Immune involvement in schizophrenia and autism: etiology, pathology and animal models. *Behav. Brain Res.* 204, 313–321. <https://doi.org/10.1016/j.bbr.2008.12.016>.
36. Yi, Y.H., Yang, Z., Han, Y.W., and Huai, J. (2017). Effects of rapamycin on clinical manifestations and blood lipid parameters in different preeclampsia-like mouse models. *Chin. Med. J. (Engl)* 130, 1033–1041. <https://doi.org/10.4103/0366-6999.204924>.
37. Chng, S.H., Kundu, P., Dominguez-Brauer, C., Teo, W.L., Kawajiri, K., Fujii-Kuriyama, Y., Mak, T.W., and Pettersson, S. (2016). Ablating the aryl hydrocarbon receptor (AhR) in CD11c+ cells perturbs intestinal epithelium development and intestinal immunity. *Sci. Rep.* 6, 23820. <https://doi.org/10.1038/srep23820>.
38. Langmead, B., and Salzberg, S.L. (2012). Fast gapped-read alignment with Bowtie 2. *Nat. Methods* 9, 357–359. <https://doi.org/10.1038/nmeth.1923>.
39. Li, D., Liu, C.M., Luo, R., Sadakane, K., and Lam, T.W. (2015). MEGAHIT: an ultra-fast single-node solution for large and complex metagenomics assembly via succinct de Bruijn graph. *Bioinformatics* 31, 1674–1676. <https://doi.org/10.1093/bioinformatics/btv033>.
40. Liu, Y., Guo, J., Hu, G., and Zhu, H. (2013). Gene prediction in metagenomic fragments based on the SVM algorithm. *BMC Bioinformatics* 14, S12. <https://doi.org/10.1186/1471-2105-14-S5-S12>.
41. Buchfink, B., Xie, C., and Huson, D.H. (2015). Fast and sensitive protein alignment using DIAMOND. *Nat. Methods* 12, 59–60. <https://doi.org/10.1038/nmeth.3176>.
42. Love, M.I., Huber, W., and Anders, S. (2014). Moderated estimation of fold change and dispersion for RNA-seq data with DESeq2. *Genome Biol.* 15, 550. <https://doi.org/10.1186/s13059-014-0550-8>.
43. Badr, H.S., Zaitchik, B.F., and Dezfouli, A.K. (2015). A tool for hierarchical climate regionalization. *Earth Sci. Inform.* 8, 949–958. <https://doi.org/10.1007/s12145-015-0221-7>.
44. Layeghifard, M., Hwang, D.M., and Guttman, D.S. (2018). Constructing and analyzing microbiome networks in R. *Methods Mol. Biol.* 1849, 243–266. https://doi.org/10.1007/978-1-4939-8728-3_16.
45. Kundu, P., Ling, T.W., Korecka, A., Li, Y., D'Arienzo, R., Bunte, R.M., Berger, T., Arulampalam, V., Chambon, P., Mak, T.W., et al. (2014). Absence of intestinal PPARγ aggravates acute infectious colitis in mice through a lipocalin-2-dependent pathway. *PLOS Pathog.* 10, e1003887. <https://doi.org/10.1371/journal.ppat.1003887>.
46. Kundu, P., Genander, M., Strååt, K., Classon, J., Ridgway, R.A., Tan, E.H., Björk, J., Martling, A., van Es, J., Sansom, O.J., et al. (2015). An EphB-Abl signaling pathway is associated with intestinal tumor initiation and growth. *Sci. Transl. Med.* 7, 281ra244. <https://doi.org/10.1126/scitranslmed.3010567>.
47. Jurek, A., Genander, M., Kundu, P., Catchpole, T., He, X., Strååt, K., Sabelström, H., Xu, N.J., Pettersson, S., Henkemeyer, M., et al. (2016). Eph receptor interclass cooperation is required for the regulation of cell proliferation. *Exp. Cell Res.* 348, 10–22. <https://doi.org/10.1016/j.yexcr.2016.08.017>.
48. Manders, E.M.M., Verbeek, F.J., and Aten, J.A. (1993). Measurement of co-localization of objects in dual-colour confocal images. *J. Microsc.* 169, 375–382. <https://doi.org/10.1111/j.1365-2818.1993.tb03313.x>.

STAR★METHODS

KEY RESOURCES TABLE

REAGENT or RESOURCE	SOURCE	IDENTIFIER
Antibodies		
Anti-Olfm4 (D6Y5A) XP Rabbit mAb	Cell Signaling Technology	Cat# 39141; RRID: AB_2650511
Anti-MUC2	Abcam	Cat# ab97386; RRID: AB_10680432
Recombinant Anti-Chromogranin A	Abcam	Cat# ab254322; RRID: AB_2910555
Rat Anti-E Cadherin	Abcam	Cat# ab11512; RRID: AB_298118
Polyclonal Rabbit Anti Human Lysozyme	Dako	Cat# A0099; RRID: AB_2341230
Anti-Phospho-mTOR (Ser2448)	Cell Signaling Technology	Cat# 2971; RRID: AB_330970
Anti-Phospho-mTOR (Ser2448) (D9C2) XP® Rabbit mAb	Cell Signaling Technology	Cat# 5536; RRID: AB_10691552
Anti-mTOR	Cell Signaling Technology	Cat# 2972; RRID: AB_330978
Anti-Phospho-S6 (Ser240/244) Ribosomal Protein (D68F8) XP® Rabbit mAb	Cell Signaling Technology	Cat# 5364; RRID: AB_10694233
Anti-S6 Ribosomal Protein (5G10) Rabbit mAb	Cell Signaling Technology	Cat# 2217; RRID: AB_331355
Anti-RFP Antibody Pre-adsorbed	RockLand	Cat# 600-401-379; RRID: AB_2209751
Mouse anti-rabbit IgG-CFL 594	Santa Cruz Biotechnology	Cat# sc-516250; RRID: AB_3661867
Anti-β-Actin (C4)	Santa Cruz Biotechnology	Cat# sc-47778; RRID: AB_626632
Goat anti-Rabbit IgG Secondary Antibody HRP conjugated	Signalway Antibody	Cat# L3012; RRID: AB_895483
Mouse Anti-Rabbit IgG-CFL 488	Santa Cruz Biotechnology	Cat# 516248; RRID: AB_3661868
Recombinant Anti-Iba1	Abcam	Cat# ab178846; RRID: AB_2636859
Anti-Doublecortin (DCX)	Cell Signaling Technology	Cat# 4604; RRID: AB_561007
Anti-MCM2	Abcam	Cat# ab108935; RRID: AB_10859977
Anti-Nestin Monoclonal Antibody	Invitrogen	Cat# 14-5843-82; RRID: AB_1907435
Rhodamine(TRITC) AffiniPure Goat Anti-Mouse IgG(H+L)	Yeasen	Cat# 33209ES60; RRID: AB_3661870
Bacterial and virus strains		
Akkermansia muciniphila	ATCC	Cat# BAA835
Bacteroides thetaiotaomicron	ATCC	Cat# 29148
Chemicals, peptides, and recombinant proteins		
BHI broth	BD Biosciences	Cat# 237500
Agar	Yeasen	Cat# 70101ES76
Soy peptone	Duoxi	Cat# J33408
Glucose Anhydrose	Macklin	Cat# G6172
N-Acetyl-D-glucosamine	Maya-R	Cat# 881023
L-threonine	Aladdin	Cat# T108221
L-cysteine	TCI	Cat# C0515
Hemin	Bidepharm	Cat# BD132990
PBS, 0.01M/pH7.2-7.4	Solarbio	Cat# P1010
KCl	SCR	Cat# 10016308
NaCl	Sangon	Cat# A501218
Na-Citrate	SCR	Cat# 10019418
KH ₂ PO ₄	Mecklin	Cat# P815662
Na ₂ HPO ₄	JiuDing	Cat# SR443
0.5M EDTA	Invitrogen	Cat# AM9260G
Sucrose	Sigma	Cat# V900116
D-sorbitol	Sigma	Cat# S1876
Dithiothreitol	Sigma	Cat# D0632
IntestiCult™ Organoid Growth Medium (Human)	STEMCELL	Cat# 06010

(Continued on next page)

Continued

REAGENT or RESOURCE	SOURCE	IDENTIFIER
PenStrep, penicillin/streptomycin	Gibco	Cat# 15140122
Bovine Serum Albumin (BSA), Fraction V	Roche	Cat# 10738328103
Advance DMEM/F12 (1x) Reduced Serum Medium	Gibco	Cat# 12634-010
Matrigel Matrix Growth Factor Reduced	Corning	Cat# 354230
GlutaMax (100x)	Gibco	Cat# 35050-061
Hepes (100x)	Gibco	Cat# 15630-080
B-27 Supplement (50x)	Gibco	Cat# 12587-010
N2 Supplement (100x)	Gibco	Cat# 17502-048
Mouse R-spondin1	R&D	Cat# 3474-RS-050
Murine Noggin	Peprtech	Cat# 250-38
Murine EGF	Peprtech	Cat# 315-09
DMSO	Sigma	Cat# D2650
PEG400	Sigma	Cat# 202398
Tween-80	Sigma	Cat# P1754
Corn oil	Sigma	Cat# C8267
Rapamycin	MedChemExpress	Cat# HY-10219
Tamoxifen	Sigma	Cat# T5648
4-Hydroxytamoxifen	Sigma	Cat# H7904
4% Paraformaldehyde	Biosharp	Cat# BL539A
Dextran Sodium Sulphate (DSS)	MP Biomedicals	Cat# 160110
Fluorescein isothiocyanate-dextran	Sigma	Cat# 46944
Methanol	SCR	Cat# 10014118
Xylene	Macklin	Cat# X820585
Citric acid, trisodium salt	Acros	Cat# C39197.36
Triton X-100	Bio-Rad	Cat# 1610407
Trizma base	Sigma	Cat# V900483
Tween-20	Bio-Rad	Cat# 1706531
Hydrogen peroxide	SCR	Cat# 10011218
DAPI staining buffer	Beyotime	Cat# C1006
Antifade Mounting Medium	Vector labs	Cat# H-1000
Phosphatase inhibitors cocktail tablets	Roche	Cat# 4906845001
Protease inhibitors cocktail tablets	Roche	Cat# 4693159001
Quick Start Bovine Serum Albumin (BSA) Standard	Bio-Rad	Cat# 5000206
Quick Start Bradford 1x Dye Reagent	Bio-Rad	Cat# 5000205
APS, Ammonium persulfate	Sangon	Cat# A100486
Acrylamide/bis-acrylamide, solution	Sigma	Cat# A7802
Sodium Dodecyl Sulfate (SDS)	Promega	Cat# H5114
Precision Plus Protein™ Kaleidoscope™ Prestained Protein Standards	Bio-Rad	Cat# 1610375
Restore Plus Western Blot Stripping Buffer	Thermo	Cat# 46430
TEMED	Macklin	Cat# N818999
Western Blotting Luminol Reagent	Santa Cruz	Cat# sc-2048
β-mercapthoethanol	SCR	Cat# 80076928
Rnase and Dnase Away	Beyotime	Cat# R0123
Fast SYBR™ Green Master Mix	Applied Biosystems	Cat# 4385612
TrypLE Express Enzyme	Thermo Fisher Scientific	Cat# 12604-013
DNase 1	Roche	Cat# 10104159001
7-AAD Viability Stain Solution	eBioscience	Cat# 00-6993-50
Y-27632 dihydrochloride	Sigma	Cat# Y0503-1M

(Continued on next page)

Continued

REAGENT or RESOURCE	SOURCE	IDENTIFIER
5-Ethynyl-2'-deoxyuridine (Edu)	Sigma	Cat# 900584
HCL	SCR	Cat# 10011008
Critical commercial assays		
click-iT Edu Alexa fluor 488 imaging kit	Invitrogen	Cat# C10337
ImmPRESS Horse Anti-Rabbit IgG Plus Polymer Kit	Vector	Cat# MP-7801
ImmPRESS Goat Anti-Rat IgG (Mouse Adsorbed) Polymer Kit	Vector	Cat# MP-7444
one step TUNEL Apoptosis Assay Kit	Beyotime	Cat# C1088
OpalTM 7-Color Manual IHC Kit	Akoya Biosciences Inc	Cat# NEL811001KT
iScript cDNA Synthesis Kit	Biorad	Cat# 1708891
High capacity cDNA Reverse Transcription Kit	ThermoFisher	Cat# 4368814
RNeasy Mini Kit	Qiagen	Cat# 74104
Rabbit specific IHC polymer detection kit HRP/DAB	Abcam	Cat# ab209101
Deposited data		
Metagenomics	This paper	NCBI SRA Database: SRP492208; SRP495394
Metabolomics	This paper	National Omics Data Encyclopedia (NODE) database: OEP005141
RNA sequencing	This paper	NCBI SRA Database: SRP494239
Experimental models: Organisms/strains		
Mouse: C57BL6J	Jackson lab	Cat# 000664
Mouse: ICR	Jackson lab	Cat# 009122
Mouse: Lgr5-EGFP-IRES-creERT2	Jackson lab	Cat# 008875
Mouse: Lgr5-2A-CreERT2-R26-tdTomato	Seishima et al. ²⁰	N/A
Mouse: C57BL/6J (Germ-Free)	GemPharmatech	Cat# N000295
Software and algorithms		
GraphPad Prism 8	GraphPad	https://www.graphpad.com/scientific-software/prism/www.graphpad.com/scientific-software/prism/
QuPath™ (v0.4.3)	QuPath	https://qupath.github.io/
Vectra3.0™ Multispectral Imaging System	PerkinElmer, USA	https://www.akoyabio.com/phenoimager/instruments/vectra-3-0/
InForm Advanced Image Analysis Software (v2.4)	PerkinElmer, USA	https://www.akoyabio.com/phenoimager/inform-tissue-finder/
LabImage software	Kapelan	https://www.kapelanbio.com/products/labimage/
Dr. TOM	BGI	https://biosys.bgi.com/
Imaris-9.5.1	Oxford Instruments	https://imaris.oxinst.cn/versions/9-5
TopScan Lite software	CleverSys	https://cleversysinc.com/CleverSysInc/csi_products/topscan-lite/
R (version 4.3.1)	N/A	https://cran.rproject.org
R studio	Posit	https://posit.co/products/open-source/rstudio/
Adobe Photoshop CS6	Adobe	https://www.adobe.com/products/photoshop.html
ZEN 3.4 software	Zeiss	https://www.zeiss.com/microscopy/en/products/software/zeiss-zen.html
Image J	Wayne Rasband	https://imagej.net/ij/
Other		
QTRAP 6500 Plus	SCIEX, USA	N/A
Waters UPLC I-Class Plus	Waters, USA	N/A
QuantStudio 1 real-time PCR system	Applied Biosystems	N/A

EXPERIMENTAL MODEL AND STUDY PARTICIPANT DETAILS

Mice

Specific pathogen free C57BL/6 mice aged 6–8 weeks were used as breeders in our experiments. Mice were gavaged with *Akkermansia muciniphila* (Am) (strain: ATCC BAA835) at a dose of 10^8 CFU/mice or vehicle (PBS) every alternative day during the entire period of pregnancy (beginning from the day the breeding was initiated). In some experiments, as outlined in the text, mice were gavaged with Am (10^8 CFU/mice) or PBS every alternative day during the entire pregnancy period while, the newborn pups from each group were subsequently exposed to either PBS or Am (10^6 CFU/mice) on alternate days starting from day-5 (this timepoint was chosen to reduce gavage associated mortality) till weaning (21 days). Mice gavaged similarly with *Bacteroides thetaiotaomicron* (Bt) (strain: ATCC 29148) served as experimental controls. Rapamycin treatment in pregnant mice was given at a dose of 0.25 mg/kg b.w. every alternate day during the entire period of pregnancy following previous protocols.³⁶ Rapamycin (MedChemExpress HY-10219) was dissolved in 1% DMSO, 5% (PEG400) and 5% Tween-80 for orogastric gavage. Experimental endpoints in individual experiments range from 3 days up to 10 months and are clearly specified in the text respectively. Similar experiments were conducted using Lgr5-EGFP-IRES-creERT2 and Lgr5-2A-CreERT2-R26-tdTomato²⁰ mice for intestinal stem cell isolation and lineage tracing studies respectively. For Cre activation, Lgr5-2A-CreERT2-R26-tdTomato mice were intraperitoneally injected with 2mg tamoxifen/mouse dissolved in 10% DMSO and 90% corn oil, 48 or 72 hours before sacrifice.

For fostering experiments, 19-day-old embryos from pregnant C57BL/6 mice, treated with either PBS or Am were isolated by C-section. These pups were revived and transferred to foster mothers (ICR mice). The pups from each group were then raised by the foster mothers until they reached 3 weeks of age (endpoint).

For the induction of colitis, 2-month-old mice born to PBS- or Am-exposed mothers were given 2.5% Dextran Sodium Sulphate (DSS) in their drinking water for 7 consecutive days. The DSS-containing water was replaced with fresh 2.5% DSS every 3 days to prevent contamination. After 7 days, the DSS-containing water was replaced with normal drinking water, and the mice were allowed to recover for an additional 7 days. Recovery rates were then assessed (endpoint).

For fecal microbiota transplantation (FMT), groups of germ-free (GF) mice (6–8 weeks old) were transplanted with fecal microbiota collected from pregnant donor mice undergoing PBS or Am treatments, at late-stage gestation (between day 16–18). Briefly, fecal pellets from 3 donor mice from each group were dissolved in sterile PBS by homogenization (using sterile plastic pestle and vigorous shaking), and each recipient mouse was immediately fed with 150 μ l of the supernatant using a sterile orogastric gavage to transplant microbiota. The conventionalization procedure was repeated on the 3rd day post initial inoculation as a booster. Breeding was set up immediately after the first dose of FMT. GF recipients conventionalized with microbiota from donors of either PBS or Am groups were housed in separate confined plastic isolators until their F1 generation reached 3 weeks of age (endpoint).

Mono-colonization of GF mice with Bt was achieved by a dose of 10^8 CFU/mice and a repeat dose of similar concentration on the 3rd day post initial inoculation as a booster. For di-colonization with Am, Bt mono-colonized mice were set for breeding and gavaged with a dose of 10^8 CFU/mice of Am every alternative day during the entire period of pregnancy. Di-colonized mice were housed in separate confined plastic isolators until their F1 generation reached 3 weeks of age (endpoint). Colonization of Bt was tested using the primers: Bt-Fw: TCGAAAGTGTGGGTATCAAACA and Bt-Rv: CTGTATATCGCAAACAGCGAGT; while Am colonization was tested using Am-Fw: CAGCACGTGAAGGTGGGGAC and Am-Rv: CCTTGCGGTTGGCTTCAGAT primers.

All mice (SPF, GF, FMT-donors and FMT-recipients and mono/di-colonized) were fed with autoclavable laboratory rodent diet P1103F-35 (energy 3.67kcal/g, SLACOM, Shanghai, China). The dietary composition for mice exposed to a high-fiber and high-protein diet (Shuyu Biotechnology, Shanghai) throughout the entire pregnancy period is outlined in [Table S1](#). However, the offspring of these pregnant mice, which were subjected to the dietary interventions (high-fiber + high-protein diet), received normal chow. Of note, all experimental mice received the same chow throughout the entire course of experiment (except the high-fiber + high-protein diet exposed mice), thus excluding any dietary influence on the microbiome composition and function. Fecal pellets were collected intermittently from the respective recipients to validate conventionalization. All protocols involving animals were carried out in accordance with institutional guidelines at Institute Pasteur Shanghai and approved by the Animal Welfare and Ethics Committee of Institute Pasteur Shanghai (protocol numbers: A2020023, A2020024, A2022004-1 and A2023025).

Human participant

Surgically resected human colonic tissue was obtained from a colorectal cancer patient (age: 64 years, sex: Male). Patient consent was formally obtained from the patient. Human sample was collected following the guidelines of the Human Ethics Committee of Hospital of Nantong University, Nantong 226001, China (Ethical approval no: 2023-K109-01).

METHOD DETAILS

Bacterial culture

Akkermansia muciniphila were grown under strict anaerobic conditions on BHI agar (BD, Sparks, MD, USA, 237500) plates containing 1.6% soy peptone (J33408-250g, Duoxi), 1.13% glucose Anhydrous (50-99-7, Macklin), 0.55% N-acetylglucosamine (7512-17-6, Maya), 0.4% L-Threonine (72-19-5, Aladdin) supplemented with 0.05% L-cysteine. *Bacteroides thetaiotaomicron* were grown under strict anaerobic conditions on BHI agar plates supplemented with 0.001% Hemin and 0.05% L-cysteine. Inoculum for mice was prepared by growing a single colony from pure culture plates of respective bacteria into the fresh media broth and subsequently

re-culturing in fresh media until they reach 0.5–0.8 OD at 600 nm wavelength. Mice were gavaged with 100 μ l of inoculum from respective bacterial suspension of 1×10^9 CFU/mL in sterile PBS.

Isolation of crypts and organoids culture

Intestinal crypts were harvested as previously described.³⁷ Briefly, small intestines were opened longitudinally, washed with cold PBS and incubated in extraction buffer (1.5mM KCl; 96mM NaCl; 27mM Na-Citrate; 8mM KH₂PO₄; 5.6mM Na₂HPO₄; 15mM EDTA) on ice for about 20 mins. The intestines were then transferred into ice cold PBS (containing 0.1% BSA and PenStep) and vortexed 5 times for 3–4 mins, each time using fresh ice-cold PBS until the crypts are visibly isolated. The crypts were then filtered through a 70 μ M cell strainer and centrifuged at 250g for 5 minutes at 4°C. Purified crypts, mixed with growth factor reduced matrigel (Corning) were then plated in 48-well plates or 8 well chambered cover-glass slides (Thermo Scientific) and cultured as previously described.³⁷ 4-Hydroxytamoxifen (1 μ M; Sigma-Aldrich) was added in Lgr5-2A-CreERT2-R26-tdTomato organoid media to induce activation of CreERT2 and consequent activation of the tdTomato cassette. Staining of EdU+ve cells in the organoids was done using click-iT Edu alexa fluor 488 imaging kit (Invitrogen™ C10337). Imaging of organoids was performed using multi-color long-time ultra-high resolution (120nm) imaging through Olympus SpinSR10 spinning disc microscope.

Human organoids and serum exposure

Peritumoral colonic tissue obtained from a colorectal cancer patient was cleaned using cold PBS and the muscle and fat tissues were removed before isolation of colonic crypts. The colonic tissues were minced using sterile scissors and the tissue fragments were incubated in extraction buffer (5.6mM Na₂HPO₄; 8mM KH₂PO₄; 96mM NaCl; 1.6mM KCl; 44mM Sucrose; 54.8mM D-sorbitol; 0.5mM Dithiothreitol; 10mM EDTA) on ice for about 30 mins. The colonic tissue fragments were then transferred into cold extraction buffer without EDTA and vortexed 5 times for 2 mins, each time using fresh extraction buffer without EDTA. The fractions containing maximum crypts are identified using a microscope, pooled and filtered through a 100 μ m cell strainer. Purified crypts, were embedded in matrigel (Corning) and cultured using IntestiCult™ Organoid Growth Medium (Human) (Catalog #06010) containing 10 μ M rho-kinase inhibitor Y-27632 (Sigma, Y0503-1M) and PenStrep. Human organoids were exposed to serum from pregnant mice (late gestation) for 24 hours. Staining of EdU+ve cells in the organoids was done using click-iT Edu alexa fluor 488 imaging kit (Invitrogen™ C10337). Organoids imaging was performed using multi-color long-time ultra-high resolution (120nm) imaging through Olympus SpinSR10 spinning disc microscope.

Intestinal Permeability Test

Mice were fasted for about 6 hours before oral gavage with FITC-dextran in PBS at a concentration of 50mg/100g body weight. After 4 hours the mice were sacrificed and blood was collected. The serum isolated from the blood was diluted with equal volumes of PBS. The concentration of FITC in serum was detected by fluorometry with an excitation of 485 nm (20 nm band width) and an emission wavelength of 528 nm (20 nm band width) using as standard serially diluted FITC-dextran (0, 125, 250, 500, 1,000, 2,000, 4,000, 6,000, 8,000 ng/ml). Serum from control mice with no FITC-dextran treatment was used to normalize the background.

Behavioral tests

Testing took place between 09:00 and 16:00 hours under low illumination by an experimenter blind to the treatment group. On the day of testing, animals were brought in sterile filtered cages to the testing room and allowed to rest for 30 minutes before testing. Test chambers were cleaned first with disinfectant and then with ethanol (70% in water) after each animal.

Open Field Test: Animals were placed individually in the center of a plexiglass open field box (60 cm \times 60 cm), and their spontaneous motor activity was video recorded for 20 minutes. The following parameters were recorded automatically using TopScan Lite software (CleverSys, Inc.) software: time spent and number of entries into the center and periphery zones.

Light Dark Box Test: the light-dark test was used to assess anxiety-related behaviour during a 10 min session in a polypropylene cage divided into two chambers by a wall with a small vestibule dividing into an illuminated chamber (30 cm \times 28 cm \times 28 cm) and a dark chamber (15 cm \times 28 cm \times 28 cm). The light zone was open, and indirectly illuminated by external lamps to a brightness of (300 Lux at the cage floor) while the dark zone was closed by a black, close-fitting lid. The mouse was placed into the light compartment and was video recorded freely exploring the apparatus for 10 minutes. The following parameters were recorded automatically using TopScan Lite software (CleverSys, Inc.) software: time spent in the dark and light zones, number of entries into each zone, latency to enter dark zone.

Elevated Plus Maze Test: The elevated plus maze test was used to test anxiety-related behavior during a 5-min session in a dark-gray glacial polyvinyl chloride apparatus comprising four arms (5 cm wide) and a central platform (7.5 cm \times 7.5 cm) elevated 60 cm above the floor. Two arms were open (78 cm) and two were closed (79 cm) with 20 cm-high walls. Mice were individually placed in the center facing an open arm and allowed to explore for 5 min. The behavior of the animal was video recorded and the following behaviors scored automatically by TopScan Lite software (CleverSys, Inc.) software: time spent in the center platform and in the open and closed arms, and number of entries into each zone.

Y Maze Test: The Y maze is used to test spontaneous alternation behavior, characterized by the tendency for mice to alternate their nonreinforced choices of Y-maze arms on successive opportunities. Each arm of the Y-maze was 31 cm long, 10 cm high, 5 cm wide. The arms converge in an equilateral triangular central area that is 5 cm at its longest axis. Each mouse was placed individually at the center of the apparatus and allowed to move freely through the maze during a 5-min session. The total number of arm entries and the

sequence of entries were video recorded to calculate the percentage of alternation and the following behaviors scored automatically by TopScan Lite software (CleverSys, Inc.) software.

Metagenomics

Metagenomic analysis was done on fecal samples collected from mothers at late-stage gestation (between day 16-18) and their pups (21 days) from PBS and Am groups as well as from the donors (mothers at late-stage gestation) and recipients (14-days post transplantation/conventionalization) of the FMT experiment.

DNA Samples: Prior to library preparation, the quality of the DNA samples was assessed on a Bioanalyzer 2100, using a DNA 12000 Chip (Agilent). Sample quantitation was carried out using Thermo Qubit 4.0 assay. Library preparation was performed according to Illumina's TruSeq Nano DNA sample preparation protocol. The samples were sheared on a Covaris S220 to ~450bp, following the manufacturer's recommendations, and uniquely tagged with one of Illumina's TruSeq LT DNA barcodes to enable library pooling for sequencing. The finished libraries were quantitated using Thermo Qubit 4.0 assay and the average library size was determined on a Bioanalyzer 2100, using a DNA 7500 chip (Agilent). Library concentrations were then normalized to 4nM, using Illumina's PhiX control library as standard. The libraries were then pooled at equimolar concentrations and sequenced in one lane on a MGI DNBSEQ-T7 sequencer in rapid mode at a read-length of 150bp paired-end.

The raw metagenomics reads were quality and adapter-trimmed using Fastp 0.36 with parameters of "Q < 20 -minimum-length 35nt". The trimmed metagenomics reads were then mapped against the mm10 mouse genome with bowtie2 2.2.5,³⁸ using "-D 20 -R 3 -N 1 -L 20 -i S,1,0.50" as its sensitivity parameters. Any reads that cannot be confidently mapped against the genome (with -un-conc switch) were separated and processed as the microbiome reads. Megahit 1.2.9 was used to perform multi-sample mixed splicing to obtain preliminary spliced contig sequences. Afterwards, Megahit 1.2.9,³⁹ was used to perform multi-sample mixed splicing to obtain preliminary spliced contig sequences, with -min-count 2 -k-min 27 -k-max 147 -k-step 12 -min-contig-length 500. Prodigal 2.60 was used to predict the ORF of the splicing results and genes with a length greater than or equal to 100 bp were selected, and translated into amino acid sequences.⁴⁰ These gene sets were then aligned against NR, KEGG, SEED and other databases with DIAMOND 0.8.20,⁴¹ with E-value < 1e-5, Score > 60. Data was visualized using R vegan package 2.5-6.

SEED-based gene functional network analysis: The gene abundance (reads) table and the SEED-based gene annotation table were imported into R (version 4.3.1, <https://cran.r-project.org>) using the R package 'data.table' (version 1.14.8, <https://cran.r-project.org/web/packages/data.table>), and merged by shared gene IDs. Only genes enriched in SEED level 1 terms showed significant difference in abundance between the PBS and Am samples, and the ones with abundance level of over 10 reads among more than 50% of the samples, were kept for downstream analysis. Differentially abundant genes (DDGs, with abs(log₂ Fold Change) > 1, adjusted P value < 0.001) between the PBS and Am groups were identified using 'DESeq2' R package (version 1.40.2).⁴² For the functional network analysis, the gene correlations in the PBS and Am samples were computed based on the abundance of each DDG using the 'HiClimR' R package (version 2.2.1)⁴³ with two-tailed tests to estimate the P value. The correlation values with absolute value >= 0.7, P value < 0.001 were retained. The functional network was visualized with the Fruchterman-Reingold layout using the 'igraph' R package (version 1.5.1).⁴⁴

Histology

Intestinal tissues from mice were Swiss rolled, fixed in 4% formaldehyde, embedded in paraffin and sectioned for histological studies. Portions of intestinal ileum were used for histological analysis in all cases. Sections (5 μm) were cut with a microtome, stained with Periodic Acid Schiff (PAS). In DSS-induced experimental colitis experiments, colonic rolls were stained for hematoxylin and eosin.⁴⁵ Slides were scanned and images were captured using Leica Image Hub at respective magnifications and processed in Adobe Photoshop CS6 (Adobe Systems incorporated).

In vivo proliferation assay

Intestinal tissues from mice were Swiss rolled, fixed in 4% formaldehyde and sectioned. To visualize proliferative cells, mice (20gms b.w.) were intraperitoneally injected with 500 μg of EdU in 100 μl sterile PBS and sacrificed 2 hours later.⁴⁶ Intestinal rolls were sectioned and stained for EdU using Click-iT Alexa Flour 488 Imaging Kit (Invitrogen), following the manufacturer's protocol.⁴⁷ Images were captured using Olympus VS120 microscope system. EdU marked cells were quantified using multi-image TIFF images through QuPath™ (v0.4.3) digital bio-image workstation. Statistical analysis was performed in GraphPad Prism 8 (GraphPad Software). P < 0.05 was considered significant.

Terminal Deoxynucleotidyl Transferase-mediated Nick End Labeling (TUNEL)

TUNEL staining was performed in the intestinal sections using the One Step TUNEL Apoptosis Assay Kit (Beyotime; C1086), according to the manufacturer's protocol. Nuclei were labeled with DAPI. Images were captured using the super-resolution microscope (ZEISS Elyra7). TUNEL-labeled cells (red fluorescence) were counted using QuPath™ (v0.4.3) digital bio-image workstation. Statistical analysis was performed in GraphPad Prism 8 (GraphPad Software). P < 0.05 was considered significant.

Immunofluorescence staining

For DCX, Mcm2 and Iba-1 staining, the brains were fixed in 4% PFA, equilibrated in 20% sucrose and sectioned in the coronal plane at 16 μm with Cryostat (LEICA). DCX was labeled with a rabbit polyclonal antibody (Cell Signaling Technology), and visualized using

Alexa Fluor 488-conjugated secondary mouse anti-rabbit antibody (SantaCruz Biotechnology). MCM2 was labeled with a rabbit monoclonal antibody (Abcam; diluted 1:500) and visualized using Alexa Fluor 594-conjugated secondary mouse anti-rabbit antibody (SantaCruz Biotechnology). Iba-1 was labeled with a rabbit monoclonal antibody (Abcam) and visualized using Alexa Fluor 594-conjugated secondary mouse anti-rabbit antibody (SantaCruz Biotechnology). Nuclei were labeled with DAPI. Hippocampal dentate gyrus imaging was performed using multi-color long-time ultra-high resolution (120nm) imaging through Olympus SpinSR10 spinning disc microscope. DCX+ cells were counted in whole dentate gyrus images of hippocampus. The obtained cell numbers were normalized by the size of dentate gyrus (DCX+ cell number/mm²). For Nestin staining mice were perfused using 4% formaldehyde, equilibrated in 20% sucrose and sectioned in the coronal plane at 16 μm with Cryostat (LEICA). Nestin was probed with a monoclonal anti-nestin antibody (Invitrogen) and visualized using Alexa Fluor 550-conjugated secondary antibody (Yeasen Biotechnology). Phospho-mTOR was probed with a polyclonal anti-p-mTOR antibody (Cell Signaling Technology) and visualized using Alexa Fluor 488-conjugated secondary antibody. Nuclei were labeled with DAPI. Images were captured using the ZEISS Elyra7 Super-Resolution microscope and analyzed by ZEN 3.4 software package. Multi-color-staining of OLFM4, Lysozyme and p-mTOR was performed on formalin-fixed and paraffin-embedded intestinal tissues using the Opal™ 7-Color Manual IHC Kit (NEL811001KT, Akoya Biosciences Inc) following the manufacturer's protocol. OLFM4 was probed with a monoclonal anti-OLFM4 antibody (Cell Signaling Technology), and visualized using Opal 570. Paneth cells were labeled with a polyclonal anti-lysozyme antibody (Dako) and visualized using Opal 540. Phospho-mTOR was probed with a polyclonal anti-p-mTOR antibody (Cell Signaling Technology) and visualized using Opal 650. Nuclei were labeled with DAPI. Images were captured using the ZEISS Elyra7 Super-Resolution microscope and ZEN 3.4 software package. Overlap coefficient was calculated according to Manders' overlap coefficient (MOC), based on an actual overlap of the signals, which represent the true degree of colocalization.⁴⁸ Statistical analysis was performed in GraphPad Prism 8 (GraphPad Software). P<0.05 was considered significant. For detection of Tomato+ve cells, sections were probed with anti-RFP polyclonal antibody (RockLand) and visualized using Alexa Fluor 594-conjugated secondary antibody (SantaCruz Biotechnology). Nuclei were labeled with DAPI. Images were captured using Olympus VS120 microscope system and the super-resolution microscope (ZEISS Elyra7). RFP+ve tracing length were measured using QuPath™ (v0.4.3) digital bio-image workstation. Statistical analysis was performed in GraphPad Prism 8 (GraphPad Software). P<0.05 was considered significant.

Multiplexed immunohistochemistry staining (mIHC)

To visualize and simultaneously quantify multiple cellular populations in the gut, we used quantitative immunofluorescence (QIF) assay based on several murine intestinal markers. Antibody validation was performed in recommended positive controls and on mouse intestinal tissues prior to multiplexed staining. Multiplexed immunohistochemistry on formalin-fixed and paraffin-embedded tissues was carried out using Opal Tyramide Signal Amplification (TSA) technology-based Opal™ 7-Color Manual IHC Kit (Cat #NEL811001KT Akoya Biosciences Inc) following the manufacturer's protocol. Briefly, the slides containing intestinal Swiss rolls underwent multiple cycles of antibody incubation, Opal™ fluorophore conjugation and retrieval. The process was conducted for multiple antibodies/fluorescent dyes, in the following order: Lysozyme/opal 540, MUC2/opal 650, Olfm4/opal 570, Chromogranin A/opal 520, E Cadherin /opal 620 and DAPI. The signal specificities of individual markers were validated using proper negative controls. After staining, coverslips were mounted using Vectashield hardset® fluorescence mounting medium (#H-1400-10, Vector Labs, Burlingame, CA) and slides were imaged in Vectra3.0™ Multispectral Imaging System (PerkinElmer, USA). Spectral unmixing for digital images was carried-out in inForm Advanced Image Analysis Software (v2.4 PerkinElmer) with earlier registered spectral libraries from single marker-stained slides along with unstained slides to normalize auto-fluorescence. Images were exported in multi-image TIFF format and analyzed for subset quantification and crypt depth measurements using QuPath™ (v0.4.3) digital bio-image workstation.

Western blotting

Tissue extracts (50–80 μg/lane) from purified crypts and hippocampal tissues were prepared in lysis buffer [10 mM Tris-HCl (pH 8), 150 mM NaCl, 1% Triton X-100, containing protease and phosphatase inhibitors (Roche)] and subjected to Western blotting. The Western blots were probed using anti-p-mTOR (Cell Signaling), anti-mTOR (Cell Signaling), anti-p-S6 (Cell Signaling) and anti-S6 (Cell Signaling). Immuno-detection with an appropriate secondary peroxidase-conjugated antibody (DAKO) was followed by chemiluminescence-based (ECL; Santa Cruz) detection using ChemiDoc XRS+ (Biorad). Protein band quantification was performed using LabImage software.

Real-time PCR

Total RNA was extracted using RNeasy mini-kit (Qiagen), and cDNA synthesis was performed using SuperScript II (Invitrogen), both following the manufacturer's protocol. The expressions of respective genes were analyzed using semiquantitative real-time PCR with SYBR Green (Applied Biosystems).⁴⁶ Following the recommendations of Applied Biosystems, the primers in [Table S2](#) were designed and tested. The sample setups always included at least four biological replicates and experimental triplicates. Data are presented as fold-change in relative gene expression normalized to β-actin.

Targeted Metabolomics

Serum samples collected from pregnant mice undergoing PBS or AM treatments, at late-stage gestation were sent to BGI (Shanghai, China) for unbiased targeted metabolomics analyses. High-performance liquid chromatography-tandem mass spectrometry

(LC-MS/MS) was used to perform high-sensitivity, wide-coverage, and high-throughput HM700-targeted quantification of 700 metabolites in these samples. Briefly, 20 μ l of serum or quality control (QC) sample solution was mixed with 120 μ l of 50% aqueous methanol, centrifuged, and the supernatant was transferred to a new tube. A standard curve was prepared by serial dilution of an HM700 mixed standard. The experimental samples, QC samples, and standards were subjected to a derivatization reaction, and the resulting compounds were diluted in HM700 diluent and centrifuged at 4000 g at 4 °C for 30 minutes. The supernatant was applied to LC-MS/MS analysis. The sample extracts were analyzed using Waters UPLC I-Class Plus (Waters, USA) equipped with QTRAP 6500 Plus (SCIEX, USA) to separate and detect the plasma metabolites. Chromatography was performed on a BEH C18 column (2.1mm x 10cm, 1.7 μ m, waters). The mass spectrometry was performed with an ESI+/ESI- source. Bioinformatics and statistical analysis were performed using BGI Dr. TOM software-based standard procedures.

Sorting of LGR5+ cells and RNA-Seq

Crypts were isolated and purified from the small intestines of Lgr5-EGFP-IRES-creERT2 mice by incubating for about 15 min at 4°C in crypt isolation buffer (1.5mM KCL, 96mM NaCl, 27mM sodium citrate, 8mM KH₂PO₄, 5.6mM Na₂HPO₄, 15mM EDTA). Purified crypts were dissociated first with TrypLE Express Enzyme (Thermo Fisher Scientific) for 15 min and then with 0.2mg/ml DNase (Roche) for 10 min at 37°C under shaking conditions. Dissociated cell suspension was passed through a 40 μ m cell strainer (Biosharp) and washed with PBS. Viable epithelial single cells or doublets were gated by forward scatter, side scatter and pulse-width parameter, negative staining for 7-ADD viability staining solution (eBioscience) and FITC. The cells were sorted by flow cytometry (Aria II, BD) and GFP^{hi}-cells were collected and RNA isolation from these cells was done using RNeasy® Mini Kit (QIAGEN). RNA quality testing, library construction, and RNA sequencing (RNA-seq) were carried out by the Beijing Genomics Institute (BGI) following standard protocols. The library products were sequenced using a DNBSEQ. Standard bioinformatics analysis was performed by the Dr.Tom, bioinformatics service of BGI. Differential expression analysis of genes was performed using the DESeq2 with FDR<0.001, parameters defined by the bioinformatics service of BGI. All original sequence datasets to be submitted to the database of NCBI Sequence Read Archive (SRA).

QUANTIFICATION AND STATISTICAL ANALYSIS

Statistical analysis was carried out in GraphPad (www.graphpad.com) Prism version 8.0.1 for Windows. Data are represented as mean \pm standard error of the mean (s.e.m.). *P calculated using the Student's t test or ANOVA with Tukey's multiple comparisons test depending on group size and mentioned wherever it is <0.05. Bioinformatics and statistical analysis for RNAseq and metabolomics were performed using BGI Dr. TOM software-based standard procedures. Number of samples (n) and the method used to test statistical significance are stated in each figure legend.